1   **Title:**

2   Single-cell resolution unravels spatial alterations in metabolism, transcriptome and

3   epigenome of ageing liver

4

5   **Authors:**

6   Chrysa Nikopoulou[1,*], Niklas Kleinenkuhnen[1,2,*], Swati Parekh[1,*], Tonantzi Sandoval[1], Farina

7   Schneider[3], Patrick Giavalisco[4], Mihaela Bozukova[1], Anna Juliane Vesting[5], Janine Altmüller[6],

8   Thomas Wunderlich[5,7], Vangelis Kondylis[3], Achim Tresch[2,7,#] and Peter Tessarz[1,7,#]

9

10   **Affiliations:**

11   1: Max Planck Research Group 'Chromatin and Ageing', Max Planck Institute for Biology of Ageing,

12   Joseph-Stelzmann-Str. 9b, 50931 Cologne, Germany

13   2: Institute of Medical Statistics and Computational Biology, Faculty of Medicine, University of Cologne,

14   Bachemer Str. 86, 50931, Cologne, Germany

15   3: Institute for Pathology, University Hospital Cologne, Kerpener Str. 62, 50937 Cologne, Germany

16   4: Metabolic Core Facility, Max Planck Institute for Biology of Ageing, Joseph-Stelzmann-Str. 9b, 50931

17   Cologne, Germany

18   5: Max Planck Institute for Metabolism Research, Gleueler Str. 50, 50931 Cologne, Germany6: Cologne

19   Center for Genomics, University of Cologne, Cologne, Germany; Berlin Institute of Health at Charité,

20   Core Facility Genomics, Berlin, Germany; Max Delbrück Center for Molecular Medicine in the Helmholtz

21   Association, Berlin, Germany.

22   7: Cologne Excellence Cluster on Cellular Stress Responses in Aging-associated Diseases (CECAD),

23   Joseph-Stelzmann-Straße 26, 50931 Cologne, Germany

24   * equal contribution

25   # correspondence: achim.tresch@uni-koeln.de, ptessarz@age.mpg.de

26

27

28

29

30 **ABSTRACT**

31 Epigenetic ageing clocks have revealed that tissues within an organism can age with different

32 velocity. However, it has not been explored whether cells of one type experience different

33 ageing trajectories within a tissue depending on their location. Here, we employed lipidomics,

34 spatial transcriptomics and single-cell ATAC-seq in conjunction with available single-cell RNA-

35 seq data to address how cells in the murine liver are affected by age-related changes of the

36 microenvironment. Integration of the datasets revealed zonation-specific and age-related

37 changes in metabolic states, the epigenome and transcriptome. Particularly periportal

38 hepatocytes were characterized by decreased mitochondrial function and strong alterations in

39 the epigenetic landscape, while pericentral hepatocytes – despite accumulation of large lipid

40 droplets – did not show apparent functional differences. In general, chromatin alterations did

41 not correlate well with transcriptional changes, hinting at post-transcriptional processes that

42 shape gene expression during ageing. Together, we provide evidence that changing

43 microenvironments within a tissue exert strong influences on their resident cells that can shape

44 epigenetic, metabolic and phenotypic outputs.

45

1

INTRODUCTION

Ageing is characterised by a general physiological decline that is accompanied by metabolic, epigenetic and transcriptional changes[1]. A common attribute for these alterations is an increased inter-individual heterogeneity as observed in large cohorts. Even on an organismal level within populations of genetically identical individuals, variability seems intrinsically inter-connected with ageing. For example, in cohorts of *C. elegans* or mice, some individuals die much earlier than others[2].

It is largely appreciated that transcriptional variability increases with age[3–5]. While whole tissue omics approaches have been important to get an insight into the uniform changes that occur on the organ level during ageing, such methods cannot investigate heterogeneity on a cellular level. It is therefore unresolved whether all cells of the same cell type in a tissue age in the same way or whether the location of the cells within a tissue matters in this context. The development of single-cell and spatial omics methods renders it now possible to obtain (spatially resolved) molecular profiles at close to single-cell resolution, thus providing promising tools for deciphering the multifaceted process of ageing[6].

The liver is a heterogeneous tissue that consists of hepatocytes arranged in repeating units of hexagonally shaped lobules. Blood flows into the lobule from portal veins and hepatic arteries at the corners of the lobules to the central veins. This architecture creates gradients of oxygen, nutrients and hormones[7]. This gradual change in the lobule's microenvironment is also referred to as liver zonation[8] and the resulting spatial division of labour is essential for the optimal function of the liver. For example, the outer highly oxygenated periportal lobule layers perform mitochondrial-dependent metabolic tasks such as *β*-oxidation whereas the low oxygen concentrations at the pericentral areas will drive glycolysis[7]. As hepatocytes are the primary cells that perform these metabolic processes and their metabolic characteristics depend on location, the liver is an attractive tissue to address the impact of location and metabolic state on the ageing trajectory within a dedicated cell type.

2

72   Here, we employed spatial transcriptomics as well as single-cell ATAC-seq (scATAC-seq) in

73   conjunction with publicly available single-cell RNA-seq (scRNA-seq) data from ageing mice to

74   address how ageing of hepatocytes is affected by zonation in the liver. One very obvious

75   phenotypic difference in the ageing and diseased liver is the deposition of fat, which is mainly

76   focused around the central vein. Using spatial transcriptomics, we report insights into the

77   molecular underpinnings of this phenotype, and additionally identify mitochondrial dysfunction

78   as a potential driver for age-related phenotypes in the periportal region of the liver. While

79   scATAC-seq can clearly separate young and old hepatocytes, unsupervised clustering

80   approaches do not separate scRNA-seq profiles based on their age. Yet, age is a relevant

81   factor for explaining transcriptional variability between cells. Together, the data presented here

82   shed light on the molecular basis of fat deposition in the ageing liver and serve as a valuable

83   resource for the hepatic and ageing community.

84

85

86   **RESULTS**

87   **Spatial Transcriptomics give insights into the zonation-specific and age-related**

88   **metabolic rearrangements.**

89   Transcriptional profiling using bulk RNA sequencing data from the Tabula Muris Consortium[9]

90   shows metabolic pathways, known to be changing in ageing[10], with the majority of genes

91   contributing to alterations in lipid metabolism (Figure S1a,b, Supplementary Table 1). Changes

92   in lipid metabolism have been described to occur during ageing and the recent development

93   of lipidomics started to identify corresponding changes in lipid profiles[11]. Liver pathologies that

94   involve fat deposition, such as non-alcoholic fatty liver disease (NAFLD) show a tendency

95   towards zonated lipid deposition around the central area[12], but we were not aware of any

96   dataset investigating lipid deposition in the ageing liver with respect to the specific zones. To

97   assess the lipid deposition around the main zones, we performed RNAScope for pericentral

98   (Cyp2e1, Glul) and periportal markers (Albumin, Cyp2f2)[13] combined with H&E (Hematoxylin

99   and Eosin) staining in liver isolated from young (3-4 months) and old (18-20 months) mice

100   (Figure 1a, S1c). Importantly, Sirius red staining showed no profound increase in liver fibrosis

101   in old livers (Figure S1c). On the contrary, Oil-red-O (O-R-O) staining (Figure S1d, upper

102   panel) and immunohistochemical (IHC) staining for PLIN2 (Figure S1d, lower panel), a protein

103   known to be enriched at the outer membrane of LDs[14], showed that large LDs accumulate

104   around the central vein in aged livers.

105   The apparent zone-dependent deposition of lipids in the ageing liver prompted us to

106   investigate the underlying transcriptional events. We used the 10X Genomics Visium Platform

107   and ran 10μm tissue cryosections from livers of two young and two old mice. The sequencing

108   metrics of the samples can be found in Supplementary Table 2. Initially, we visualized the

109   normalized spatial gene expression of the zonation markers Cyp2f2, Cyp2e1 and Glul in young

110   and old liver (Figure 1b). Based on the expression distribution of these marker genes, spatial

111   transcriptomics was able to resolve central and portal areas.

112
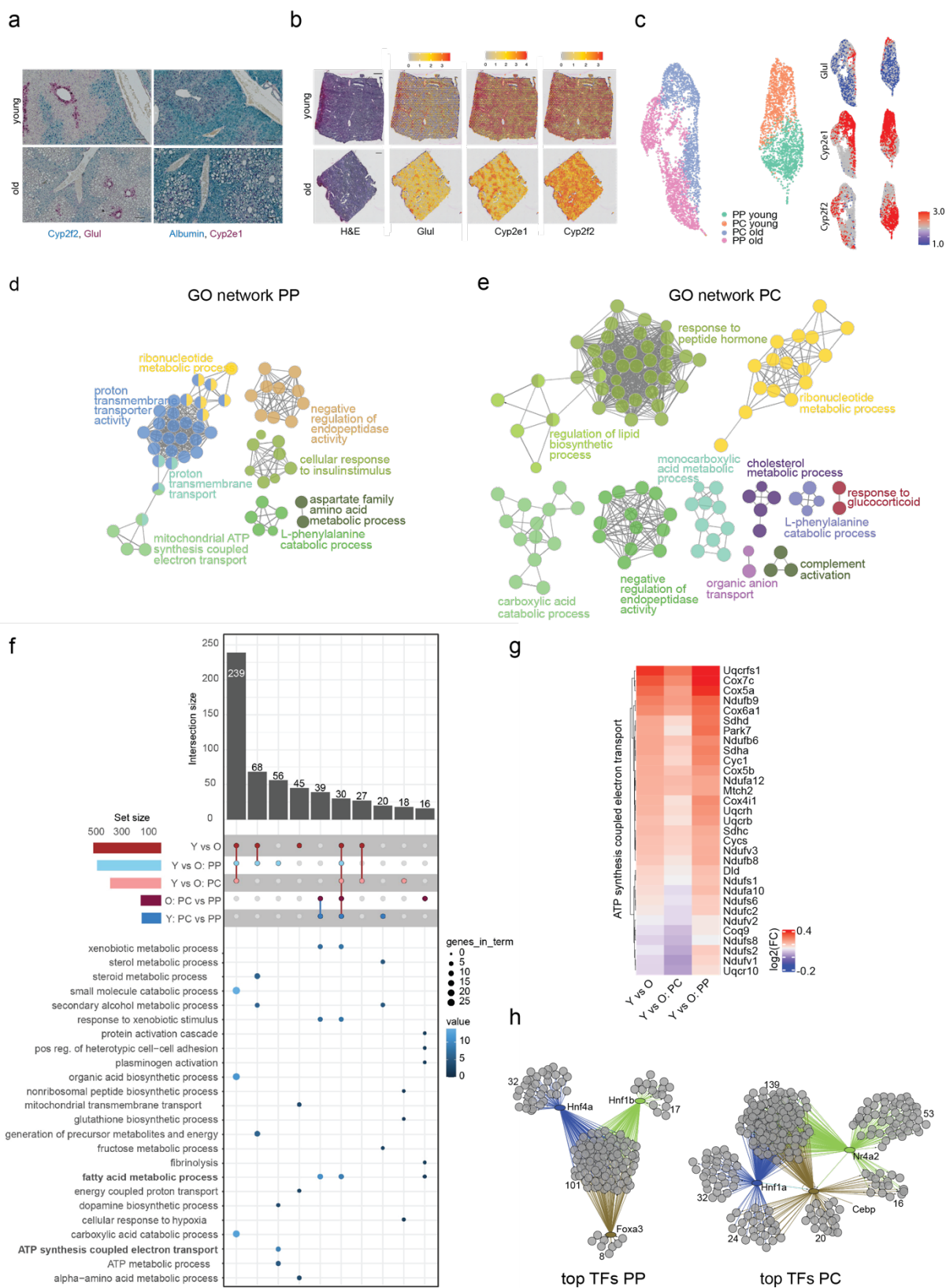
Figure 1: Age-related and zonation-specific transcriptional alterations. a) RNAscope of zone-

specific marker genes Glul (magenta, upper panel), Cyp2f2 (cyan, upper panel), Cyp2e1 (magenta,

lower panel) and Albumin (cyan, lower panel) in paraffin-embedded liver sections from young (3 month

116   old) and old (18 month old) mice. Scale bar = 100 μm. b) H&E staining of one young (upper panel) and

117   one old (lower panel) liver specimen used for spatial transcriptomics (Scale bar=500 μm) and plots

118   showing the expression levels of Glul, Cyp2f2 and Cyp2e1 indicated by colour. The colour gradient

119   represents normalised gene expression. c) UMAP projection of the spatial data, colour-coded are the

120   different zones and ages (left panel) and the expression of Glul, Cyp2e1 and Cyp2f2 (right panel). d),

121   e) GO network calculated using ClueGO for differentially expressed genes in the periportal (based on

122   Supplementary Table 3 - for details, see Method section) (d) and pericentral (e) zone of the ageing liver.

123   f) UpSet plot showing the number of differentially regulated genes (top) and pathways (bottom) in the

124   indicated categories (Y=young, O=old, PC=pericentral, PP=periportal). g) Heatmap with hierarchical

125   clustering of differentially expressed genes from the indicated pathways selected from f). g)

126   Transcription factor activity prediction from the age-dependent differentially expressed genes by the

127   iRegulon app in Cytoscape (based on Supplementary Table 3 - for details see Methods section). For

128   each zone, the top predicted TFs are shown as well as their interaction to regulate transcripts. Numbers

129   indicate the genes in every cluster.

130

131

132   Principal Components analysis showed that spots from each slide cluster; spots from the two

133   young liver slides overlap, while spots from the two old slides separate (Figure S1e).

134   Therefore, to guard against batch effects, we integrated young and old datasets individually,

135   first using canonical correlation analysis[15] and analysing zonal expression effects. Then, we

136   merged all datasets using the same strategy. To assess whether the sample separation

137   reflected gene expression differences based on age or were mostly due to a potential batch

138   effect, we used the loadings calculated in the PCA and intersected those with a recently

139   published resource, in which global ageing genes were defined organismal and tissue-wide[16].

140   The majority of the genes that contributed to the first principal component were part of the

141   liver-specific global ageing genes (Figure S1f). To perform differential analysis of the PP and

142   PC zones of the liver tissue, we assigned spots to pericentral and periportal groups based on

143   Cyp2e1 and Cyp2f2 expression levels (Figure 1c, Methods). We used a two-part, generalised

144   linear hurdle model[17] to identify gene expression changes between young and old liver in

145   general, but also specifically in periportal and pericentral region upon ageing (Supplementary

146   Table 3). We performed GO enrichment using the ClueGo plugin for Cytoscape[18,19] for the

147   age-related changes in the two zones. While the periportal region was characterized by

148   changes in mitochondrial respiration and proton transport as well as amino acid metabolism

149   (Figure 1d), ontologies in the pericentral zone were enriched for terms related to lipid

150   biosynthesis and carboxylic acid catabolic processes (Figure 1e). Common for both zones

151   were changes in ribonucleotide metabolism and response to peptide hormones, such as

152   insulin (Figure 1d,e). To further zoom into the differences of the zones, and to identify

153   commonly and zone-specifically deregulated genes, we represented the data as an UpSet plot

154   (Figure 1f). This analysis confirmed the notion of zone-specific alterations. The periportal area

155   showed age-related expression changes of genes encoding for members of the electron

156   transport chain, for example an age related decrease in Uqcrfs1 (cytochrome b-c1), which

157   catalyses the electron transfer from ubiquinol to cytochrome c[20], and Cox7c or Cox5a that

158   drive oxidative phosphorylation[21] (Figure 1g). On the other hand, the pericentral area showed

159   a signal of hypoxia, which might be caused by the previously reported changes in liver

160   vascularisation upon ageing[22]. Finally, we wanted to understand whether the transcriptional

161   changes were driven by a dedicated set of transcription factors. We used the iRegulon app

162   within Cytoscape[18,23] and visualised the top three most significant TFs (NES >4) based on

163   age-dependent differential expression within the two zones. Shared between the zones is

164   Hnf1, which has been shown to regulate many hepatic genes[24]. Genes in the periportal area

165   were predicted to be regulated by Hnf4a and Foxa3 (Figure 1h). Hnf4a is a master regulator

166   during hepatic differentiation and plays an important role during liver regeneration[25], similarly

167   to Foxa3[26]. In addition, Hnf4a has recently been shown to possess anti-proliferative capacity

168   and thus protects against hepatocellular carcinoma[25]. On the other hand, genes in the

169   pericentral zone were predicted to be regulated by Cebp and Nr4a2 (Figure 1h), two TFs that

170   regulate glucose and lipid metabolism[27,28]. Taken together, spatial transcriptomics revealed

171   that ageing is accompanied by zonation-specific metabolic rewiring, which is driven by a

172   network of dedicated transcription factors.

173 **The ageing liver is characterised by lipid remodelling and loss of spare respiratory**

174 **capacity in periportal mitochondria**

175 The spatial transcriptomic data suggested age-related metabolic alterations that depend on

176 the location of cells with respect to central or portal regions. To gain more insight into the

177 metabolic alterations, we first performed lipidomics to characterise the changes in lipid

178 metabolism within the ageing liver. This approach allowed us to address not only storage and

179 membrane lipids, but also to analyse levels of cardiolipins and ubiquinones to further

180 investigate the observed alterations in mitochondrial metabolism.
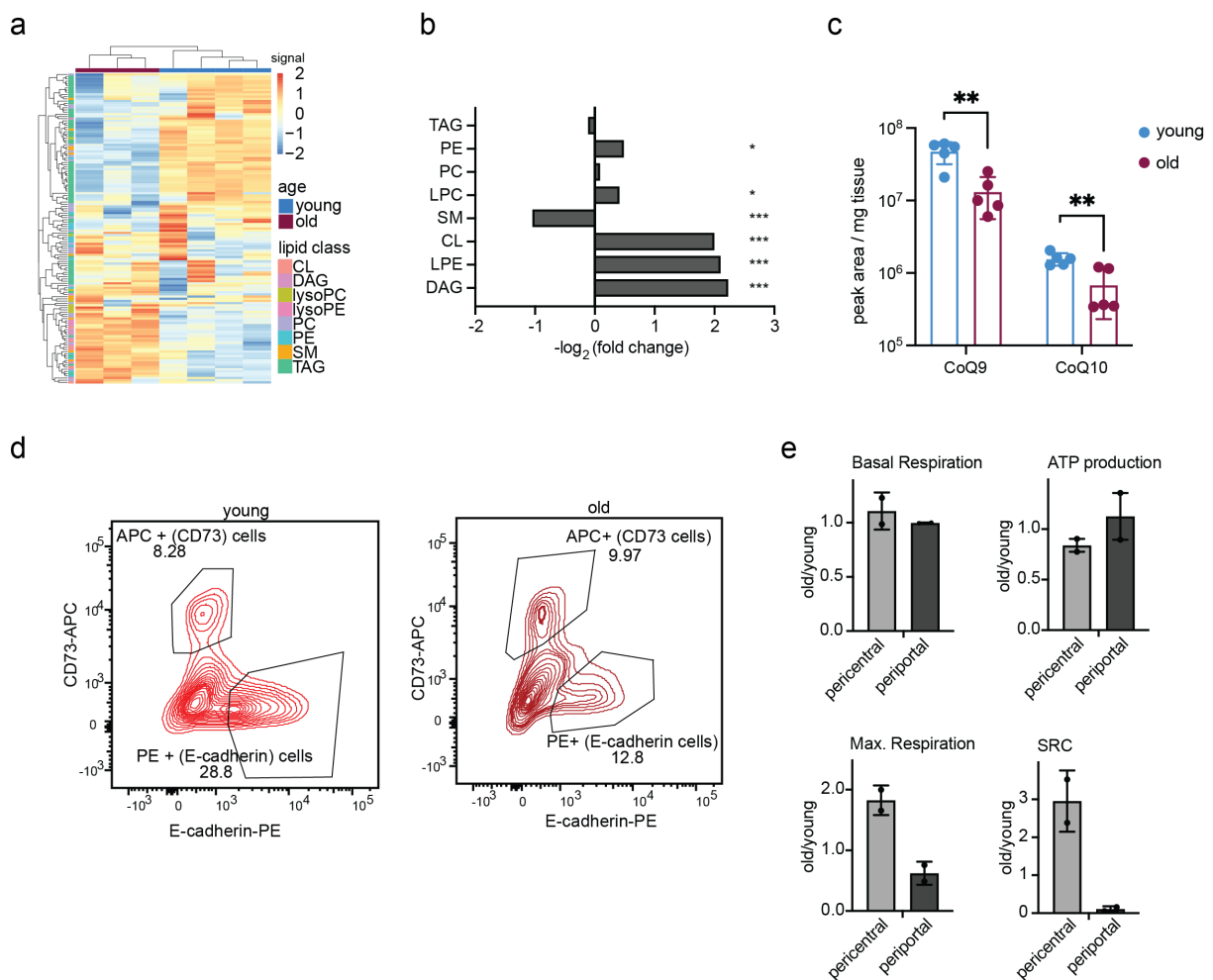
181

182 **Figure 2: Lipid remodelling and alterations in mitochondrial metabolism in the ageing liver.** a)

183 Heatmap with hierarchical clustering of lipid datasets derived from 3 old and 4 young mouse livers,

184 showing the differentially expressed classes of lipids. Hierarchical clustering was performed using

185 LipidSig [29] based on data available in Supplementary Table 4. b) Bar plot of the log-fold changes in lipid

186 classes expressed in old vs. young liver. Fold changes and significance (*p-value<0.05, ***p-

187   value<0.001) were calculated using LipidSig based on data available in Supplementary Table 4. c) Bar

188   plot showing the expression of Ubiquinones CoQ9 and CoQ10 in young and old liver. Statistical

189   significance was determined using a two-sample t-test (**p-value<0.01). d) Exemplary FACS profiles of

190   sorted hepatocytes based on CD73 (pericentral) and E-Cadherin (periportal). e) Mitochondrial function

191   as measured by Seahorse Mitochondrial Stress kit (parameter on top of graph) expressed as old vs

192   young and pericentral-periportal. N=2 (per N, one or two young and two old mice were sorted and

193   averaged). Error bars represent the SEM.

194

195

196   We extracted lipids from livers of young and old mice. PCA (Figure S2a) and differential

197   abundance analysis of the most significantly changed lipids (Figure 2a, Supplementary Table

198   4) showed a strong lipid remodelling for most of the major lipid classes. While we did not

199   observe an overall increase in triacylglycerides (TAGs), we noted a significant increase in the

200   levels of lysoPE (LPE) and lysoPC (LPC) (Figure 2b), which might stem from the remaining

201   serum in the liver as those lipids are enriched in extracellular fluids [30]. Importantly, we noted

202   a strong increase in diacylglycerides (DAGs) and a decrease in sphingomyelin (SM) (Figure

203   2b), pointing towards changes in membrane fluidity[31,32] and lipid-mediated signalling. Indeed,

204   an increase in DAGs as well as a decrease in SMs has been linked to an increase in insulin

205   insensitivity, a well-known hallmark of ageing[33,34] and a pathway that was also evident in the

206   spatial transcriptomics data (Figure 1d,e). We then focused on mitochondria-related lipids. A

207   significant increase in all cardiolipins (CL) measured (Figures 2b, S2b) indicated changes in

208   the composition of mitochondrial membranes and hence the function of mitochondrial inner

209   membrane proteins, including the electron transport chain (ETC)[35]. This hypothesis was also

210   supported by the observation that ubiquinones, lipids that transfer the electron between the

211   different complexes of the ETC, were strongly down-regulated with age (Figure 2c). These

212   findings in combination with the spatial transcriptomics data supported the hypothesis of age-

213   dependent mitochondrial changes. As the spatial transcriptomic data and the lipidome analysis

214   pointed towards a strong impact on mitochondrial metabolism, we wanted to investigate this

215   phenotype in more detail, particularly in a zone-specific manner. In order to do this, we used

216   a previously published protocol[36] to sort hepatocytes into pericentral and periportal upon

217   perfusion of the liver (Figure 2d, S2c). This approach depends on the zonation-dependent

218   expression of E-cadherin (periportal) and CD73 (Nt5e, pericentral)[36] and was able to separate

219   pericentral and periportal hepatocytes as judged by expression of Glul and Cyp2f2 (Figure

220   S2d). First, we measured mitochondrial content in the two zones in an age-dependent manner,

221   which was variable across different animals and zones, but largely unaltered with age (Figure

222   S2e). Finally, we performed Seahorse analysis using the mitochondrial stress kit to assess

223   mitochondrial function. While basal respiration and ATP production changed only mildly with

224   age, we observed a striking reduction in the maximal and thus, spare respiratory capacity

225   (SRC) in periportal hepatocytes (Figure 2e). On the other hand, pericentral hepatocytes

226   showed an increase in maximal respiration. Loss of SRC sensitizes the cells to surges in ATP

227   demand[37] and it has been proposed that SRC can be used as a measure of mitochondrial

228   health[38]. Taken together, spatial data, lipidomics and bioenergetics measurements point

229   towards an age-dependent decrease in hepatic mitochondrial fitness and function, specifically

230   in the periportal zone of the liver.

231

232   **Chromatin accessibility in mouse liver carries a hepatocyte ageing signature**

233   Having defined the transcriptional, lipid and functional alterations that occur within the

234   periportal and pericentral zones of the ageing liver, we next wanted to investigate if the

235   differences in phenotype and transcriptome might be explained by an underlying change on

236   the epigenetic level. Therefore, we performed scATAC-seq using the 10x Chromium platform.

237   We profiled 4838 nuclei prepared from three young liver tissues and 3361 nuclei from three

238   old liver tissues. Sequencing metrics can be found in Supplementary Table 3. In order to

239   identify cell types and their accessibility profiles, we combined the young and old datasets and

240   subsequently analysed them together using cisTopic[39]. Clustering according to cell-to-cell

241   similarity using UMAP identified several cell clusters. Most of the clusters showed intermixing

242 between young and old cells. However, the biggest cluster showed a clear separation between

243 the two age groups (Figure 3a).
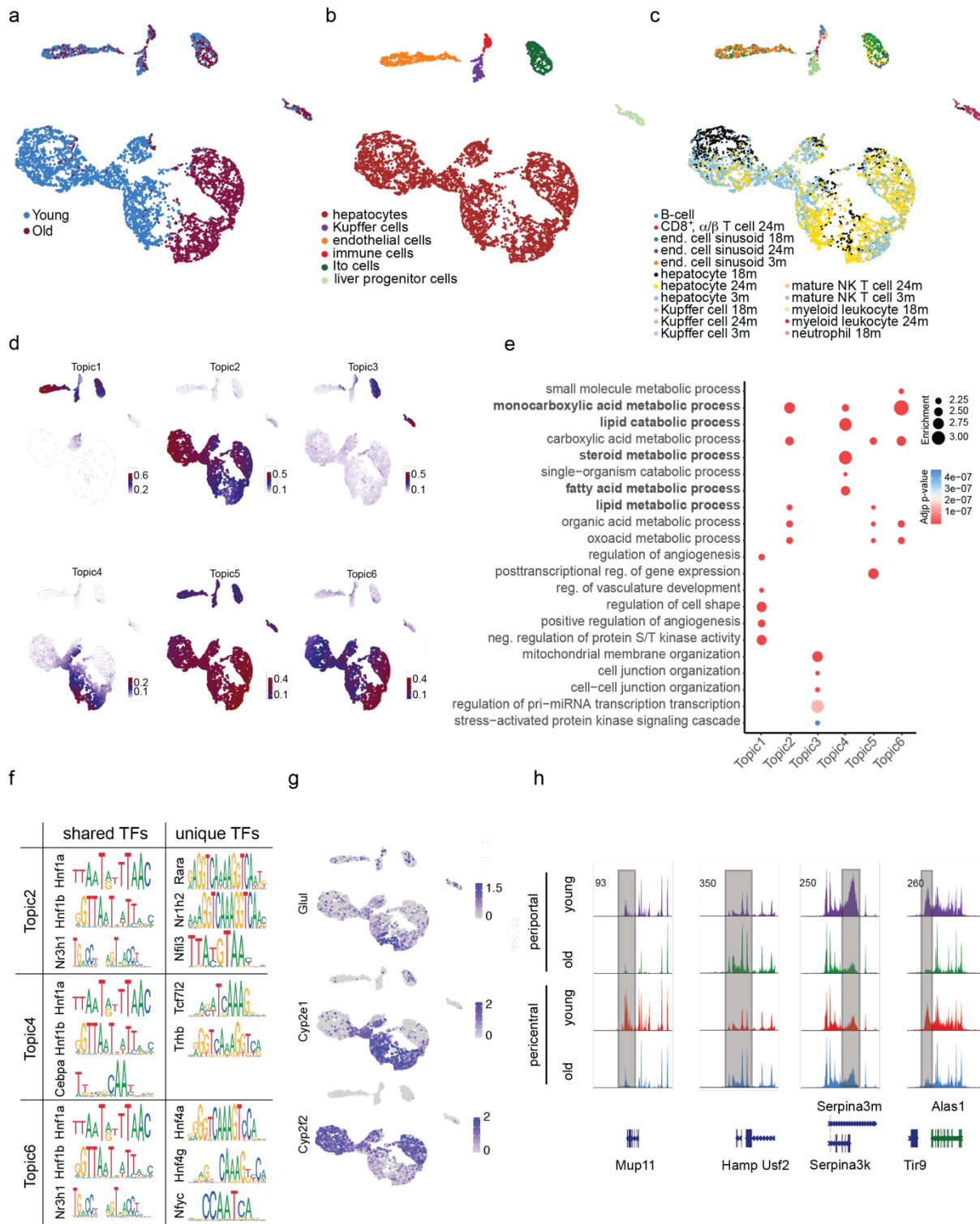
Figure 3: Differential chromatin accessibility in aged liver hepatocytes. a-c) UMAP projection of scATAC-seq data of mouse liver nuclei. a) Different colours represent liver cells from young and old age groups identified using cisTopic. b) Different colours represent different cell types based on imputed

248   marker gene activity (see also Supplementary Figure S3C). c) Different colours represent different cell

249   types predicted with cell type assignment using the FACS data of the TMS [9] d) cisTopic identified six

250   different topics. Colour code of the UMAPs is according to the normalised topic score for each cell. e)

251   GO term analysis of the 6 different topics. Highlighted are liver-associated metabolic processes. f)

252   Shared and unique transcription factor (TF) motifs corresponding to the ''hepatocyte'' topics 2, 4 and 6.

253   g) UMAP projections as in A. Colour code corresponds to the imputed gene activity of zone-specific

254   genes Glul, Cyp2e1 (pericentral) and Cyp2f2 (periporal). h) Exemplary tracks of differentially accessible

255   sites between pericentral and periportal hepatocytes upon ageing. The grey bar indicates altered

256   regions.

257

258   This behaviour was confirmed by a complementary clustering using Signac[40] (Figure S3a). To

259   identify cell types, we inferred transcriptional activity from the respective promoter

260   accessibility, as described previously[41]. We used known marker genes[13,42] and CellMarker

261   (http://bio-bigdata.hrbmu.edu.cn/CellMarker/) to infer the cellular identity of each cluster. We

262   were able to resolve all expected cell types of the liver, except for cholangiocytes (Figure 3b,

263   S3b-c). We were not able to distinguish different immune cell types since their marker genes'

264   imputed activity was ambiguous (Figure 3b, S3b,c). In line with the observation that the livers

265   were not fibrotic, we did not observe a significant increase in immune or hepatic stellate cell

266   numbers based on the scATAC-seq profiles or detected a specific inflammatory signal.

267   Notably, based on the marker gene profiles, the only cluster clearly separated by age was the

268   hepatocyte one (Figure 3a,b, S3a,b). Regions that changed accessibility with age encoded for

269   genes involved in pathways such as glucose homeostasis and fat-cell differentiation (Figure

270   S3d). To further validate our chromatin-state-based cell type assignment, we predicted cell

271   types of our scATAC-seq data with FACS-based scRNA-seq (Smart-seq2) data from the TMS

272   consortium[9]. The integration largely confirmed our cell type prediction (Figure 3c). However,

273   we noticed that particularly hepatocytes were not predicted clearly in different age groups.

274   Next, we made use of the inferred *cis*-regulatory topics that underlie the Latent Dirichlet

275   Allocation (LDA) used by cisTopic[39] and assigned those topics to the individual clusters. Most

276   topics referred to specific cell clusters. Four topics were enriched in the hepatocyte cluster

277   (Figure 3d). In line with the predicted cell types, GO terms associated with the hepatic topics

278   centred around lipid and xenobiotic metabolism, the epithelial topic around angiogenesis and

279   vasculature development, whereas the other topics were mostly associated with regulatory

280   terms (Figure 3d). Interestingly, topics 2 and 6 correspond to young and old hepatocytes,

281   respectively, whereas topic 4 was shared between the two age groups. Topics were further

282   exploited to predict enriched transcription factor motifs. Here, we particularly focused on the

283   three hepatic topics (Figure 3f, Supplementary Table 5). In topics 2, 4 and 6 well-known

284   hepatic transcription factors were predicted, such as Hnf1a,b (see also Figure 1h). Each topic

285   also contained its unique set of transcription factors that were specifically predicted to topic-

286   defining regions. In topic 2, which was enriched predominantly in the young hepatocytes, we

287   identified unique TFs to be Nr1h2, which is involved in steroid metabolism as well as Nfil3,

288   which controls Per1 and Per2 and is thus involved in circadian rhythm. Recent work has

289   highlighted the importance of the circadian clock during the ageing process, and changes in

290   the clock dynamics are particularly altered in the ageing liver[43]. The shared topic 4 was

291   characterised by TFs involved in b-catenin and Wnt signalling, Tcf7l2 and Trhb, which is linked

292   to b-catenin production through thyroid signalling[44]. Finally, topic 6, which is enriched in old

293   hepatocytes, contained Hnf4a as a predicted unique TF. These unique transcription factors

294   predicted for each of the topics implied very specific regulation of metabolic and signalling

295   pathways with age. In general, the enriched transcription factor motifs were in good agreement

296   with the prediction based on the zone-specific and age-dependent differential expression

297   (Figures 1h and 3f, Supplementary Table 5). The apparent age-dependent separation

298   between topics 2 and 6 and their respective enrichment in young or old liver prompted us to

299   investigate whether liver zonation might be associated with the topics' separation. To test this,

300   we imputed the gene activity of Glul, Cyp2e1 and Cyp2f2. Remarkably, there is a very clear

301   separation in the scATAC-seq feature plots (Figure 3g). Using the apparent activity level of

302   these three marker genes, we concluded that topic 4 represented the pericentral region,

303   whereas topic 2 described the chromatin state for young periportal hepatocytes and topic 6

304 encompassed mostly old hepatocytes. The loss of a clearly defined periportal cluster is

305 interesting and might be connected to the change in mitochondrial metabolism. Changes in

306 mitochondrial metabolism have been shown to perturb stem and somatic cell function in

307 ageing[45,46] and may lead to dysfunction of hepatocytes and other resident liver cells in the

308 periportal area. The differences in accessibility between the zones with respect to peak

309 enrichment can also be seen in other representative gene loci (Figure 3h). Taken together,

310 scATAC-seq is able to reveal changes in the epigenome of single-cells and can resolve

311 zonation-specific differences in chromatin states.

312

313 **Specific Cidea expression in the periportal zone is driven by chromatin architectural**

314 **changes**

315 How do chromatin alterations connect to the transcriptional program to drive age-related

316 phenotypes? To address this question in more detail, we initially inspected the differentially

317 expressed genes (periportal - 544; pericentral 429) that were changed with age. Intriguingly,

318 we identified two members of the Cide gene family (Cidea and Cidec, or Fsp27) to be

319 upregulated specifically in old pericentral hepatocytes (Figure 4a,b). Cideb on the other hand

320 was expressed across both ages and zones. We used this gene family as paradigm to

321 understand the connection between chromatin, transcription and phenotype as the expression

322 showed a very clear distribution. In addition, all three Cide proteins have been shown to bind

323 to LDs and to modulate LD dynamics[47–49]. Overexpression of Cidec in hepatocytes was

324 sufficient to generate large LDs[48,50] and using electron microscopy, we found that the median

325 size of LDs increased 4-fold with age (Figure 4c), which correlated well with the increased

326 pericentral expression of Cidea and Cidec. We then turned to our scATAC-seq dataset and

327 probed whether there was an underlying alteration in accessibility at the Cidea locus,

328 potentially explaining the increase in expression. Indeed, we observed a specific age-

329 dependent increase in accessibility at the Cidea locus (Figure 4d). Co-accessibility analysis

330 using Cicero[51] also identified the enhanced usage of a potential intronic enhancer within Cidea

331 as marked by H3K27ac (Figure 4d).

332
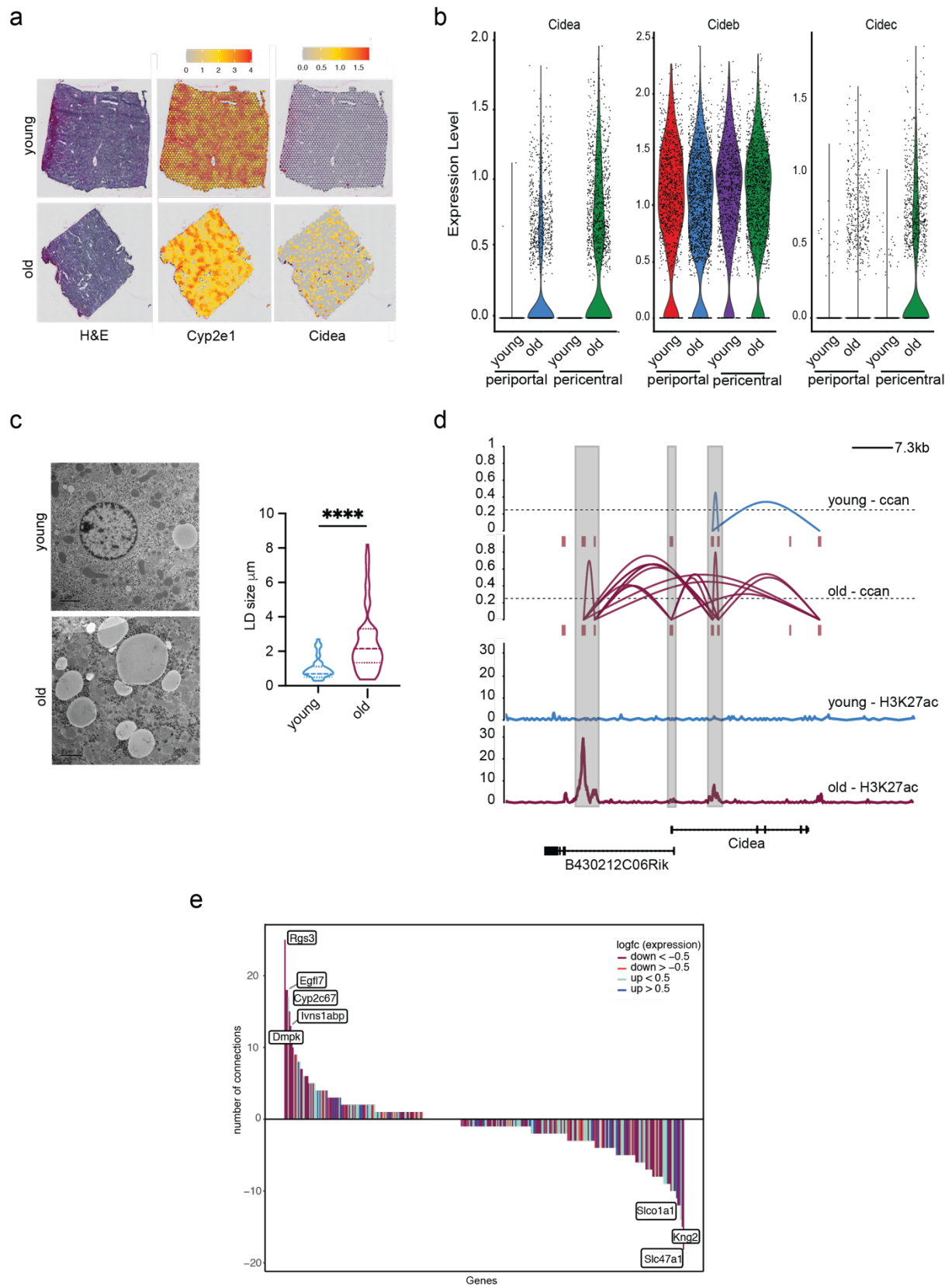
Figure 4: Connection between chromatin and transcriptional alterations in the ageing liver. a)

H&E staining of one young (upper panel) and one old (lower panel) liver specimen used for spatial

transcriptomics and a plot showing the expression level of Cidea. Please note that H&E stain and

336   Cyp2e1 plots are identical to Figure 1b and used here for reference only. The colour gradient represents

337   normalised gene expression. b) Violin plots indicating the expression levels of Cidea, Cideb and Cidec

338   across pericentral and periportal regions in young and old liver. c) Transmission electron micrograph of

339   lipid droplets (LDs) of young and old liver tissue. Representative images at 3000x, scale bar = 2 µm.

340   ImageJ quantification of the mean LD diameter size in µM from ten randomly selected photos from a

341   young (LD n=104, mean=0.8771) and ten from an old (LD n=88, mean=2.611) mouse specimen.

342   Statistical significance was determined using an unpaired two-tailed t-test; ****p-value<0.0001. d) Ccan

343   values based on Cicero [51] prediction of co-accessibility (upper panel) and the enhancer mark H3K27ac

344   (lower panel) at the Cidea locus in young and old mouse liver. Highlighted in grey are potential enhancer

345   and promoter regions from Cidea and its associated antisense long non-coding RNA, respectively. e)

346   Age-related changes in co-accessibility of loci identified using spatial transcriptomics. Y-axis shows the

347   differences in predicted contact points between young and old hepatocytes. Colour of the graphs

348   highlight direction of gene expression change as taken from the spatial transcriptomics data

349   (Supplementary Table 3) between young and old.

350

351   Given the apparent correlation between locus opening, potential enhancer engagement and

352   transcription output at the Cidea locus, we next asked whether changes in co-accessibility

353   might be a good predictor for differential gene expression on a global scale. We used the list

354   of 482 differentially expressed genes between young and old and calculated the difference in

355   chromatin accessibility for those genes (Figure 4f, Figure S4). In line with previous reports [52],

356   we did not detect a general correlation between an increase in co-accessibility and

357   transcription, indicating that co-accessibility is not a determinant for transcription. We noted

358   as well that in many cases the levels of H3K27ac did not change with age, indicating that

359   enhancer marking and co-accessibility do not necessarily go hand-in-hand (Figure S4). Taken

360   together, integration of scATAC- with scRNA-seq data confirms that alterations in chromatin

361   states are linked to gene expression differences. However, on a global level, we observed a

362   disconnect between chromatin alterations and transcriptional output, suggesting some

363   decoupling of chromatin states and transcription with age.

364

Cellular heterogeneity in gene expression but not in chromatin states increases with age

The observation that co-accessibility and transcription were not correlated in general (Figure 3f) and the finding that scRNA-seq data did not fully identify the age of cells during cell type prediction (Figure 3c) suggested that there is a decoupling between chromatin architecture and steady-state levels of mRNA in ageing hepatocytes. To identify the underlying reason for this observation, we investigated the decoupling between chromatin and the transcriptome. We initially projected the available data on liver tissue from the Tabula Muris senis consortium as a UMAP, which was generated using either the 10x Genomics platform (droplet data) or using flow cytometry and Smart-seq2 (FACS data). Consistent with the outcome of the cell type prediction, the clustering based on scRNA-seq data did not resolve the different age groups, while it clearly separated the different liver tissue cell types (Figure 5a,b). This effect can also be observed in a PCA (Figure 5c) and remained apparent when focussing exclusively on hepatocytes (Figure 5d). Such a lack of ageing signature during clustering can be observed in other reports as well[53,54]. A few studies have linked organismal and cellular ageing to transcriptional variability and cell-to-cell gene expression heterogeneity[3,55]. Thus, we wondered if an increase in cell-to-cell heterogeneity would potentially mask any underlying transcriptional ageing signature in scRNA-seq data. For simplicity, we initially focused on the major cell type of the liver, hepatocytes. First, we fit a linear model for the first three PCs with age, taking into consideration biological independent experiments in the form of mouse identity (two mice per condition) as a confounding factor (Figure S5a). We calculated the adjusted R^2 to quantify how well each PC explained age (Figure 5e) which remains under 25%. However, the noise explained as a sum of residual squares significantly increased in old cells (Figure 5f, Methods). Together, this analysis indicated that on a global level, only ~22% of the expression patterns (variance) could be explained by age and the heterogeneity of hepatocytes strongly increased with age. To assess this in all other liver-resident cell types, we fit a linear model taking into consideration cell type as an additional variable. Noise increased in all cell types with the notable exception of B cells, which showed a decrease in noise with age (Figure S5b).

17
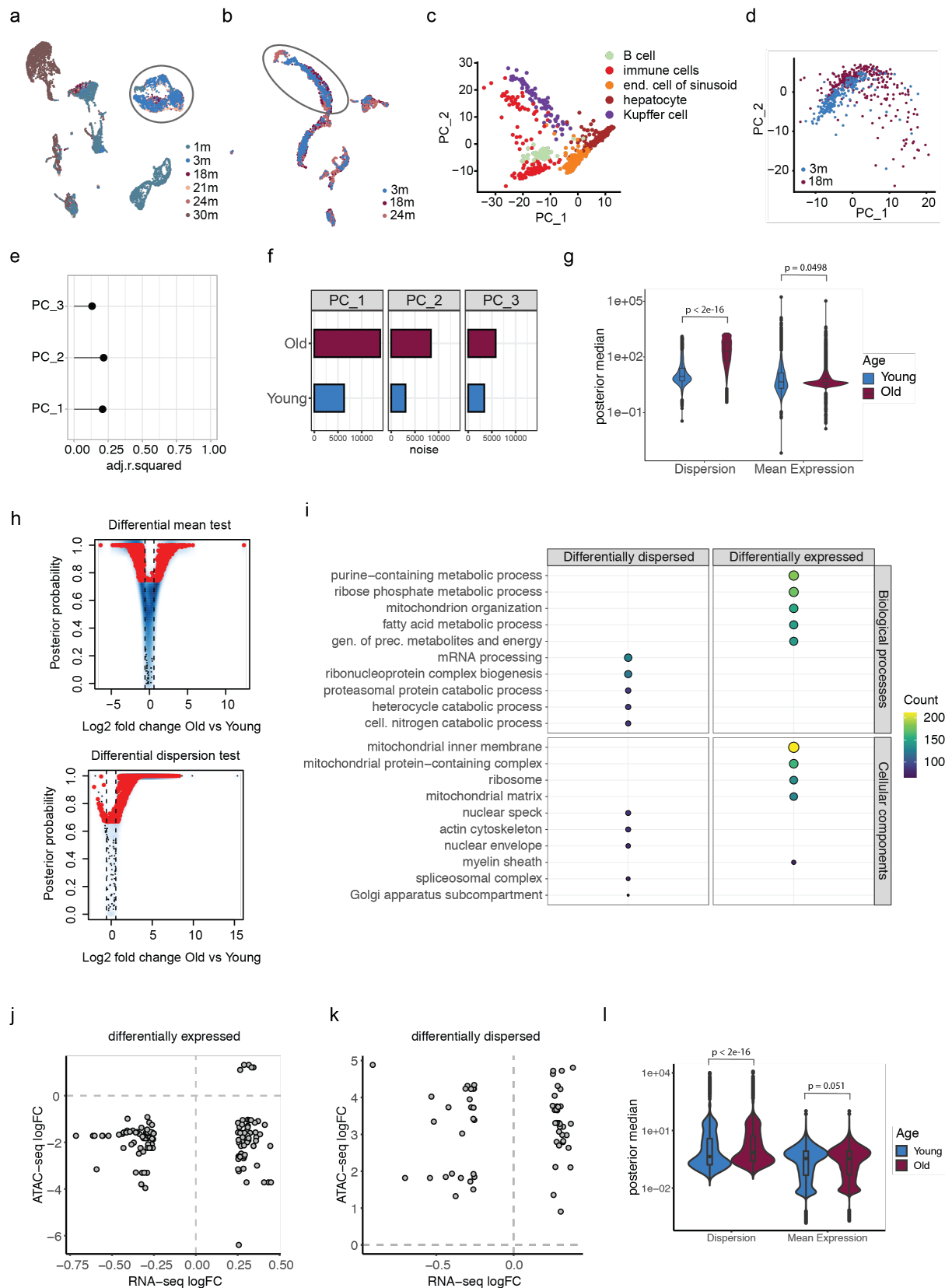
Figure 5: Transcriptional variability in hepatocytes increases with age. UMAP projection of Tabula Muris Senis (TMS) male a) 10x Genomics-based and b) FACS data coloured by age. Hepatocytes are marked with a circle. c) PCA projection of TMS male FACS data coloured by cell types and d)

397   hepatocytes coloured by age. e) Adjusted R^2 of the linear model fit of age and mouseID with the first

398   three PCs (see Figure S4A). f) The sum of residual squares for each linear model fit to the first three

399   PCs colored by age g) The posterior medians of mean expression (mu) and over-dispersion (delta)

400   parameters estimated by a regression model from BASiCS coloured by age. P-values were calculated

401   using a Welch Two Sample t-test. h,i) Log2 fold changes (x-axis) of significantly differentially expressed

402   and over-dispersed genes with the differential accessibility log2 fold changes (y-axis) measured from

403   scATAC-seq data. j) scATAC-seq gene activity matrix was used to estimate mean expression (mu) and

404   over-dispersion (delta) parameters using a regression model from BASiCS colored by age. P-values

405   were calculated using a Welch Two Sample t-test. k) Differential expression and variability was

406   determined between young and old hepatocytes. For each gene, the difference in mean expression and

407   over-dispersion is estimated as log2 fold-change (x-axis) and the posterior probability (y-axis) where

408   the red highlighted genes are significantly differentially expressed or dispersed. l) Top biological

409   processes (upper panel) and cellular components (lower panel) enriched in the differentially dispersed

410   (left) and differentially expressed (right) genes (Supplementary Table 6).

411

412   To identify genes that contributed to the age-dependent increase in noise, we used a

413   regression model implemented within BASiCS [56,57]. As shown in our previous analysis, the

414   overall distribution of mean expression remained similar while dispersion was observed to be

415   significantly higher in old cells, as suggested by the median posterior estimates of young and

416   old hepatocytes (Figure 5g). By this means, we were able to compare the differential variability

417   between young and old cells for the genes with similar mean expression. The differential test

418   obtained 5545 and 6537 genes significantly differentially expressed and dispersed,

419   respectively (Supplementary Table 6).

420   The expression difference was found to be nearly symmetrical, with 2448 up- and 3097 genes

421   down-regulated in old cells. With respect to variability, virtually all (6487 of 6537) genes

422   showed significantly higher dispersion in old cells (Figure 5h). We further filtered the

423   differentially over-dispersed genes for minimum 5% detection rate in each age group and

424   mean overall expression 5 to account for low expression or detection rate, which retained 2020

425   significantly over-dispersed genes in old hepatocytes. Strikingly, differentially expressed and

426   dispersed genes showed a clear functional separation with respect to pathways affected

427   (Supplementary Table 6). GO enrichment analysis showed that an increase in cell-to-cell

428   variability was associated with genes involved in mRNA processing RNP complex biogenesis

429   (Figure 5i), indicating that genes involved in gene expression regulation showed a particular

430   increase in variability with age. On the other hand, differentially expressed genes were

431   enriched for GO terms that deal with metabolic processes, translation and mitochondrial

432   organisation (Figure 5i). This finding was supported by the similar results from KEGG pathway

433   enrichment (Figure S5c). When compared to the bulk RNA-seq data (Figure S1a,b), the over-

434   dispersed genes contributed to 27.06% of the differentially expressed genes and 32.4% of the

435   dispersed genes overlapped with the global ageing genes[16]. Finally, we carried out the same

436   analysis with the TMS Droplet and FACS data of female hepatocytes at 3 and 18 months of

437   age. We observed very similar effects in ageing female hepatocytes regardless of the scRNA-

438   seq approach (Figure S5d). The overall dispersion was higher in aged cells and additionally,

439   the functional network was found to be the same with >75% of the genes also overlapping

440   between the datasets.

441   The cell type prediction of scATAC-seq data with the TMS scRNA-seq data did not resolve

442   cell type age. Because of this apparent decoupling of chromatin state and transcription, we

443   next correlated differential expression and dispersion in RNA with differential accessibility in

444   chromatin. We did not observe any correlation between RNA expression changes and

445   chromatin states (Figures 5j,k). Finally, we decided to investigate if chromatin itself would

446   show an increase in dispersion with age and performed BASiCS on the gene activity matrix of

447   the scATAC-seq data (for details see Materials and Methods). In contrast to scRNA-seq, we

448   did not observe an apparent increase in dispersion with age (Figure 5i), suggesting that

449   chromatin states are less heterogeneous than the transcripts. This difference in the dispersion

450   might also be one underlying reason for the observed decoupling between RNA and chromatin

451   states in the single-cell data. In summary, we observed a very strong increase in cell-to-cell

452   variability over age in the regulatory gene network, potentially masking mean expression

453   differences and hindering the ageing signature from being detected by single-cell gene

454   expression analysis.

455   **DISCUSSION**

456   The question of how the direct microenvironment of a cell within a tissue affects the ageing

457   trajectory has not been extensively explored. A few studies investigated the role of the

458   microenvironment, particularly on the fate of tissue-resident stem cells, in which age-

459   dependent perturbations of e.g. the vascular niches trigger the loss of functional hematopoietic

460   stem cells and osteoprogenitors[58]. Indeed, general attrition of vascularisation has been

461   recently reported occurring in multiple organs, including the liver[22] indicating that tissue

462   microenvironments experience profound alterations with age. This is in line with the

463   observation that ageing is accompanied by a decline in blood flow in the liver[59]. Given the

464   importance of the vascular system in setting up the division of labour of hepatocytes, the liver

465   represents an ideal tissue to address the consequences of tissue organisation and location on

466   one cell type.

467   Next to the insights into the connection of micronenvironmental changes and metabolic as

468   well as epigenomic changes in the ageing liver, the data represent a valuable resource for

469   researchers interested in liver organisation. While the scATAC-seq data will allow the

470   interrogation of chromatin states in most of liver-resident cell types, the spatial transcriptomics

471   data will mostly give insight into hepatic functions as the hepatocyte are dominating the

472   transcriptional profiles on the spots. However, manual inspection of marker cell types indicates

473   that also the spatial data can be used to interrogate non-parenchymal cells, particularly

474   Kupffer, endothelial and stellate cells (Figure S6).

475   The most apparent and macroscopic alteration with ageing to liver physiology is the

476   accumulation of large LDs in a zonated pattern, with the bulk of LDs being localised in

477   hepatocytes around the central vein of the liver lobule. Using spatial transcriptomics we

478   explored the age-dependent changes that occur within the central to portal axis of the liver

479   lobule. Interestingly, we identified members of the Cide gene family to be predominantly

480   upregulated in the central area of the liver lobule. Cidea, Cideb and Cidec are important

481   regulators of LD dynamic and growth. Indeed, an increase in expression of Cidec has been

482   shown to lead to growth of LDs[60], suggesting that the increase in Cidea and Cidec expression

483   might be one underlying reason for the increase in LD size with age. The changes in Cidea

484   expression are also encoded in the epigenome. As our scATAC-data provided enough

485   resolution to investigate zonation- and age-dependent differences, we could show that the

486   locus encoding for Cidea is remodelled with age and co-accessibility increased. The presence

487   of H3K27ac indicated that during ageing, an intronic enhancer is associated with the

488   pericentral increase of Cidea expression in hepatocytes. Such an increase of expression in

489   Cidea and Cidec has also been linked to the development of hepatic steatosis[61,62] and

490   prolonged hepatic lipid storage can lead to metabolic dysfunction in the liver and inflammation.

491   Ultimately, this development can lead to advanced forms of non-alcoholic fatty liver disease

492   (NAFLD)[63]. Thus, it is no surprise that ageing is the most common cause for the progression

493   of NAFLD.

494   Interestingly, the strong accumulation of large LDs in the pericentral region did not go hand-

495   in-hand with major chromatin rearrangements. In fact, pericentral hepatocytes from young and

496   old liver were called to belong to one topic only, indicating that their chromatin states were

497   similar. On the other hand, young and old periportal hepatocytes differed sufficiently enough

498   in their chromatin state to be enriched for different topics. Our lipidomic and spatial

499   transcriptomic analysis might provide an explanation for the apparent difference in chromatin

500   architecture in periportal hepatocytes. Cardiolipins and ubiquinones were altered strongly in

501   aged cells. Together with measurements of mitochondrial respiratory capacity, the results

502   indicated a change in efficiency of the electron transport chain and thus, ATP production,

503   particularly in the periportal region of the liver. As periportal cells are exposed to high levels of

504   oxygen due to their position close to the artery, they would usually rely on respiration. A

505   decrease in vasculature[22] and blood flow[59] might therefore have stronger consequences on

506   metabolic status in these hepatocytes than pericentral ones. A profound change in

507   mitochondrial metabolism might have direct consequences on chromatin. Indeed, several

508   studies have already connected changes in mitochondrial metabolism with alterations in

509   chromatin structure[64–66]. In support of the hypothesis that a decrease in vasculature leads to

510   changes in liver oxygenation, the spatial transcriptomics highlighted hypoxic signalling

511   changed with age, specifically in the central region of the lobule.

512   Spatial transcriptomics and the scATAC data both showed a clear signature of ageing in

513   hepatocytes. On the other hand, we noted that the scRNA-seq provided by the Tabula Muris

514   Senis consortium[9] was not able to cluster cells based on ageing. Even in hepatocytes, age

515   explained only around 25% of the variance in the data. This low impact of ageing on clustering

516   in scRNA-seq data can also be observed in other tissues in the Tabula Muris senis dataset

517   and in a few studies that were published recently[53,54]. In addition, while cell type prediction of

518   the scATAC data worked well using scRNA-seq, different ages were distributed fairly evenly

519   across the young and old hepatocyte clusters. This indicated a global decoupling of chromatin

520   and RNA, which we confirmed by correlating changes in accessibility and gene expression.

521   RNA-sequencing measures the steady-state level of mRNA, thus the technology would not be

522   able to distinguish between changes in the synthesis and post-transcriptional regulation of

523   mRNA[67]. Intriguingly, genes involved in post-transcriptional processing are among the top-

524   dispersed genes, suggesting that this layer of gene expression regulation might be

525   deregulated and more stochastic with age. One part of this layer would be mRNA splicing and

526   indeed, there have been several reports over the last years that the process of splicing is

527   strongly impacted by age and might itself contribute to ageing[68–70]. Totally unexplored as of

528   now is the role of mRNA stability and storage with age. The decoupling of chromatin state and

529   transcription is reminiscent of the decoupling of mRNA and protein levels with age[71]. Together,

530   these data suggest that there is a progressive loss of cohesion between the different layers of

531   gene expression that might contribute to the ageing process.

23

MATERIALS AND METHODS

Mice

C57BL/6N male young (3-4 months) and old (18-22months) old mice were bred and maintained in the mouse facility of Max Planck Institute for Biology of Ageing following ethical approval by the local authorities. The lights are controlled by timers and set a photoperiod of 12 hours of light from 6 am until 6pm (with a 15min twilight period). The room temperature is 22 +/- 2°C and the relative humidity 50 +/-5 %. All mice were fed with a standard diet ssniff M-Haltung, phyt.-arm (gamma irradiated).

Immunohistochemistry

Livers were excised post-mortem and fixed directly into 4% PFA for 24hrs at 4°C, washed twice with 1XPBS, embedded into paraffin blocks and cut into 5μm sections. For Oil-Red-O staining and spatial transcriptomics, freshly-dissected liver tissues were frozen in Tissue-Tek OCT compound (Sakura) and cut into 7μm and 10μm cryosections, respectively.

For IHC stainings, sections of paraffin-embedded samples were deparaffinised by immersion of the slides into the following buffers; 20 min in Xylol, 2 min. 100% EtOH, 2 min. 96% EtOH, 75% EtOH and 1x PBS and washed three times with H_2O for 5 min each. Endogenous peroxidase was quenched by immersion for 15 min in peroxidase blocking buffer (0.04 M NaCitrate pH 6.0, 0.121 M Na2HPO4, 0.03 M NaN3, 3% H_2O_2). After three washes with tap water, slides were subjected to heat-induced epitope retrieval with 10 mM NaCitrate, 0.05% Tween-20, pH 6.0, washed 5 min with 1X PBS, blocked 60 min with Blocking buffer + 160 μl/ml AvidinD and incubated with primary antibodies diluted (1:200 Plin2) in blocking buffer + 160 μl/ml Biotin overnight at 4°C. After three 5 min washes with PBST the samples were incubated with the secondary antibody 1:1000 diluted in blocking buffer for 1 h at room temperature, followed by three 5 min washes with PBST and incubation for 30 min with 1x PBS + 1:60 Avidin D + 1:60 Biotin. After three 5 min washes with PBST the samples were stained with 1 drop of DAB chromogen in 1 ml Substrate buffer, washed with 1X PBS and counterstained with Hematoxylin for 4 min, washed with tap water and distilled H2O and

559   dehydrated 1min in each buffer; 75% EtOH, 96% EtOH, 100% EtOH, Xylol and mounted with

560   Entellan.

561   **H&E staining**

562   Following deparaffinization, slides with tissues washed with distilled and tapped water and

563   stained with Hematoxylin for 5 min, followed by 5 washes in tapped water and staining with

564   Eosin Y for 3 min, followed by 3 washes with tap water, dehydration and mounting in Entellan.

565   **Oil-red-O and Sirius Red staining**

566   Oil-Red-O and Sirius Red staining were used to visualize neutral lipids and collagen,

567   respectively, and were performed according to standard procedures. Oil-Red-O staining was

568   performed on 7-µm-thick frozen liver sections that were fixed in 4% paraformaldehyde for 10

569   min, followed by staining with 0.3% Oil-Red-O (Sigma) in isopropanol/water (60:40 vol/vol) for

570   15min. Sirius red was performed on deparaffinized liver sections that were incubated for 1h at

571   RT in Picro Sirius Red solution (ab150681, Abcam), followed by washes in acetic acid and

572   alcohol solutions.

573   **RNAscope 2.5 HD Duplex**

574   Liver tissue was placed in a cassette, fixed in 4%paraformaldehyde (PFA) dissolved in

575   phosphate-buffered saline (pH 7.4) for 24hrs at 4°, washed twice with 1XPBS, and embedded

576   into paraffin blocks. 7µm thick sections were processed as described below. Detection of

577   *Cyp2f2* (Cat No. 451851), *Alb* (Cat No. 4437691), *Cyp2e1* (Cat No. 402781-C2) and *Glul* (Cat

578   No. 426231-C2) mRNA was performed using a chromogenic *in situ* hybridization technique

579   (RNAscope™ 2.5 HD Duplex Assay, Advanced Cell Diagnostics) according to the

580   manufacturer's instructions. RNAscope® 2.5 Duplex positive control probes PPIB-C1 and

581   POLR2A-C2 (Cat No. 321651) were processed in parallel with the target probes. All incubation

582   steps were performed using the ACD HybEz hybridization system (Cat No. 321462). Sections

583   were mounted on SuperFrost Plus Gold slides (ThermoFisher), dried at RT, briefly rinsed in

584   autoclaved Millipore water, air-dried, baked at 60°C for 1hrs and deparaffinized. Afterward,

585   slides were treated with hydrogen peroxidase for 10 min. and submerged in Target Retrieval

586   (Cat No. 322000) at 98.5-99.5°C for 30 min, followed by two brief rinses in autoclaved Millipore

587   water. A hydrophobic barrier was then created around the sections using an ImmEdge

588   hydrophobic barrier pen (Cat No. 310018). Sections were incubated with Protease Plus (Cat

589   No. 322330) for 30 min. The subsequent hybridization, amplification and detection steps were

590   performed according to the manufacturer's instructions (2.5 HD Duplex Detection kit

591   (Chromogenic), Cat No. 322500). Sections were counterstained with 50% Hematoxylin

592   staining and mounted with VectaMount permanent mounting medium (Cat No. H-5000).

593   **Microscopy**

594   Immunohistochemistry, stainings and RNA scope images were taken using a Nikon Eclipse

595   Ci microscope, with a colour camera.

596   **Liver perfusion and flow cytometry**

597   Livers were dissociated using the Miltenyi liver perfusion kit (beta-test version) following the

598   manufacturer's instructions. The isolated hepatocytes were washed two times with staining

599   buffer (1x PBS, 2mM EDTA, 0.5%BSA) and 1-7million hepatocytes were stained with 1:50

600   FcX, 1:100 PE-anti-E-cadherin, 1:100 APC-anti-CD73 for 1hr at room temperature. Cells were

601   washed two times with staining buffer, cells were filtered through a 100um strainer dead cells

602   were excluded with DAPI. Cells were sorted using a BD FACSARIA IIIU or Fusion Cytometer

603   and 130um nozzle. The data were analysed using the BD FACSDiva and FlowJo softwares.

604   **Mitochondrial function measurement**

605   Mitochondrial function was evaluated by measuring the Oxygen Consumption Rate (OCR)

606   with the Seahorse XFe96 Extracellular Flux Analyzer (Agilent). XFe96 cell culture plates were

607   coated with Collagen-I (40 µg/ml) overnight at 4°C and then washed 2x with 1X DPBS before

608   6,000 murine primary hepatocytes were seeded onto each well. Cells were cultured overnight

609   in DMEM+GlutaMAX containing 10% FBS and 1x PenStrep under humidified conditions at

610   37°C with 5% CO_2. Cells were washed 2x with assay media composed of XF DMEM medium

611   (pH 7.4) supplemented with glucose (10 mM), pyruvate (1 mM) and glutamine (2 mM). Cells

612   were cultured in assay media and incubated for 1h at 37 °C in a non-CO_2 incubator. The

613   Seahorse XF Mito Stress test was used to measure the OCR response after the sequential

614 injection of oligomycin (1.0 µM), FCCP (1.0 µM) and Rot/AA (0.5 µM), according to the

615 manufacturer's instructions. The data were normalised to cell numbers.

616 **Genomic DNA extraction and qPCR for mitochondrial content**

617 Cells were trypsinised and genomic DNA was extracted using the NucleoSpin Tissue XS,

618 Micro kit for DNA (REF 740901.50). Real time PCR was performed with primers specific to

619 the cyto-b mitochondrial locus (fw: TCCGATATATACACGCAAACG, rv:

620 ATAAGCCTCGTCCGACATGA) and results were nomalised to total genomic DNA using

621 primers for actin promoter locus (fw: TGCCCCATTCAATGTCTCGG, rv:

622 ATCCACGTGACATCCACACC).

623 **mRNA extraction and qPCR for Cyp2f2 and Glul expression**

624 To verify the relative abundance of expression of the respective markers of the sorted cells,

625 CD73+ pericentral and E-cadherin+ periportal cells were isolated with flow cytometry (see

626 methods above) from 3 individual (1 young and 2 old) mice and mRNA was extracted with the

627 Dynabeads™ mRNA DIRECT™ Purification Kit (61011 Thermo Fisher Scientific). Reverse

628 transcription was performed with the Maxima H Minus Reverse Transkriptase (EP 0751

629 Thermo Fisher Scientific) and the cDNA was used for qPCR with primers for Cyp2f2 (fw:

630 CTTCCTGATACCCAAGGGCAC, rv: CTGAGGCGTCTTGAACTGGT) and Glul (fw:

631 CCACCGCTCTGAACACCTT, rv: TGGCTTGGACTTTCTCACCC). The results were

632 normalised to Actin expression (fw: ACCGGTGCAGAGACATTGGAGTTCAAC, rv:

633 GTCGACTCAGATCCCGAGGCAGAGTC).

634 **Lipidomics**

635 *Lipid extraction from liver tissue samples or liver duct organoids*

636 For the lipidomic analysis of liver tissue, 20 mg of snap-frozen tissue samples were

637 homogenised using pre-cooled (liquid N_2) metal balls (5 mm diameter) in a Qiagen Tissue

638 Lyser for 1 min at 25 Hz. The pulverized tissue was resuspended in1 ml pre-cooled (-20°C)

639 extraction buffer (MTBE (methyl tert-butyl):MeOH 75:25 [v:v]), containing 0.2 µL of EquiSplash

640 Lipidomix as an internal standard. The re-suspended samples were homogenised for

641 additional 5 min at 15 Hz in the TissueLyser.

642   After efficient tissue lysis, the samples were incubated for additional for 30 min on a

643   thermomixer at 1500 rpm and at 4°C. To remove precipitated material from the samples, the

644   Metal balls were removed and all samples were centrifuged for 10 min at 4°C and21.000 x g.

645   The supernatants was transferred to a new tube and 500 µl H_2O:methanol 3:1 [v:v] were added

646   before further incubating the extracts for additional 10 min at 1500 rpm and 15°C on a

647   thermomixer. After this final incubation step the polar and lipid phases were separated in a 10

648   min centrifugation step at 16.000 x g and 15°C. . The upper phase, MTBE-phase was

649   transferred to a new tube and stored with the obtained insoluble pellets at -80°C for lipidomic

650   analysis and protein extraction and quantification (BCA).

651   *Liquid Chromatography-High Resolution Mass Spectrometry-based (LC-HRMS) analysis of*

652   *lipids*

653   The stored (-80°C) lipid extracts were dried in a SpeedVac concentrator before analysis and

654   lipid pellets were resuspended in 200 µL of a UPLC-grade acetonitrile: isopropanol (70:30

655   [v:v]) mixture. Samples were vortexed for 10 seconds and incubated for 10 min on a

656   thermomixer at 4°C. Re-suspended samples were centrifuged for 5 min at 10.000 x g and 4°C,

657   before transferring the cleared supernatant to 2 ml glass vials with 200 µl glass inserts. All

658   samples were placed in an Acquity iClass UPLC sample manager at 6°C. The UPLC was

659   connected to a Tribrid Orbitrap HRMS, equipped with a heated electrospray ionization (HESI)

660   ion source (ID-X, Thermo Fischer Scientific).

661   Of each lipid sample, 1 µl was injected onto a 100 x 2.1 mm BEH C_8 UPLC column, packed

662   with 1.7 µm particles. The flow rate of the UPLC was set to 400 µl/min and the buffer system

663   consisted of buffer A (10 mM ammonium acetate, 0.1% acetic acid in UPLC-grade water) and

664   buffer B (10 mM ammonium acetate, 0.1% acetic acid in UPLC-grade acetonitrile/isopropanol

665   7:3 [v/v]). The UPLC gradient was as follows: 0-1 min 45% A, 1-4 min 45-25% A, 4-12 min 25-

666   11% A, 12-15 min 11-1% A, 15-18 min 1% A, 20-18.1 min 1-45% A and 18.1-22 min re-

667   equilibrating at 45% A. This leads to a total runtime of 22 min per sample.

668   The ID-X mass spectrometer was operating either for the first injection in positive ionization

669   mode or for the second injection in negative ionization mode. In both cases, the analyzed

670   mass range was between m/z 160-1600. The resolution (R) was set to 120.000, leading to

671   approximately 4 scans per second. The RF lens was set to 60%, while the AGC target was

672   set to 250%. The maximal ion time was set to 100 ms and the HESI source was operating with

673   a spray voltage of 3.5 kV in positive ionization mode, while 3.2 kV were applied in negative

674   ionization mode. The ion tube transfer capillary temperature was 300°C, the sheath gas flow

675   60 arbitrary units (AU), the auxiliary gas flow 20 AU and the sweep gas flow was set to 1 AU

676   at 340°C.

677   All samples were measured in a randomized run-order and targeted data analysis was

678   performed using the quan module of the TraceFinder 4.1 software (Thermo Fischer Scientific)

679   in combination with a sample-specific in-house generated compound database. Peak areas

680   of each peak were normalized to the internal standards from the extraction buffer and to either

681   the fresh weight of the tissue or the protein concentration of the organoids.

682   **Spatial transcriptomics**

683   *Tissue and library preparation*

684   Liver specimen from 2 young and 2 old mice were cryopreserved and sections of 8 mm x 8

685   mm x 10μm specimens. Libraries were prepared using the Visium Spatial Gene Expression

686   solution from 10x Genomics using 30 minutes permeabilization time. Libraries were prepared

687   according to the manufacturer's instruction and sequenced on an Illumina NovaSeq 6000.

688   Sequencing data was initially quality controlled and pre-processed using the 10X Genomics

689   CellRanger framework.

690   *Dimensionality reduction and individual analysis of datasets*

691   Young and old liver tissue slides were analyzed individually in R (V. 4.0.0) using the Seurat

692   package (V. 4.0.4)[41]. Count matrices were normalized and scaled using the *SCTransform*

693   function with standard parameters. Relative gene expression visualization of known hepatic

694   pericentral and periportal marker genes on the spots of the tissue slides was performed with

695   the *SpatialFeaturePlot* function.

696   *Dataset integration*

697   To assess batch effects between tissue slides, we merged the processed slides using the

698   *merge* function and normalized and scaled without any further batch correction. Principal

699   component analysis for Figure 2B was performed on the 2000 most variable features. The top

700   50 genes associated with the first principal PCA component were visualized with the

701   *VizDimLoadings* functions and intersected with the hepatocyte specific aging genes list from

702   Ref. 14[16]. Integration of young and old liver tissue slides was performed in a stepwise manner

703   as an integration of all datasets together would remove all potential differences between young

704   and old datasets. First, the pre-processed young and old tissue slide datasets were integrated

705   separately per age group using canonical correlation analysis described in [15]. Second, both

706   combined datasets were merged and filtered for spots to have at least 1000 and at most 7000

707   genes expressed. Subsequently, the joined count matrix was scaled and normalized together

708   using the *NormalizeData* and *ScaleData* function.

709   *Dimensionality reduction of integrated datasets*

710   We performed principal components analysis on the preprocessed data (*RunPCA* function).

711   The first 10 principal components covered most of the data set's variance, and were

712   considered a good approximation to the data as assessed by an elbowplot (*Elbowplot*

713   function). The first 10 principal components, therefore, served as input to UMAP for further

714   dimension reduction and visualization. Known canonical liver zonation marker genes were

715   visualized with the *Featureplot* function.

716   *Differential expression testing between young and old liver tissue slides*

717   Differential expression testing was done by using the *FindMarkers* function. Genes had to

718   show at least an average $\log_2$-fold change of ±0.25 to be considered for testing. Testing was

719   performed using the *MAST* library by[17]. Bonferroni correction was applied for multiple testing

720   adjustments of p-values. Go-term enrichment analysis for combinatorial categories was

721   performed with the *enrichGO* function from the *clusterProfiler* library[72]. Results were

722   summarised using REVIGO (http://revigo.irb.hr/)[73]. Heatmap visualization of genes from

723   categories of interest was done with pheatmap[74]. Genes of GO-terms were extracted from the

724   *org.Mm.eg.db* library [75]. $\log_2$ fold changes were calculated using the *FoldChange* function.

Cytoscape

The Cytoscape[18] apps ClueGo[19] and iRegulon[23] were used to calculate gene ontology networks and transcription factor predictions, respectively. All differentially expressed genes in old (Supplementary Table 4) were used as input for all analysis. ClueGo parameters were as follows: Biological Pathways were selected as ontologies and only pathways with pV $\leq$ 0.001. GO Tree Interval was between 6 and 12. Cluster #1 was set at 2 minimum genes that represented 5% of genes, while the network connectivity was set at 0.4. iRegulon was run using Mus musculus MGI symbols using the following motif collection: 10k (9712PWMs). Putative regulatory regaion as well as motif ranking database were set as 20kb centered around TSS. NES scores for all TFs reported were > 4.

Liver tissue preparation for scATAC-seq

Liver nuclei (n=4) were prepared from frozen tissue specimens by crushing and dounce homogenising the tissue in 1 ml EZbuffer (SIGMA) (20 strokes with loose and a tight pestle, respectively) and spun 5 min at 300 g. The pellet was incubated on ice for 20 min in EZ-buffer supplemented with DNAseI NEB M0303S (4 units/ml) and 1X DNAseI buffer. Equal volume of EZ-buffer was added and samples were spun 5 min at 500 g and incubated again 10 min on ice in EZ-buffer supplemented with DNAseI NEB M0303S (8 units/ml) and 1X DNAseI buffer. Equal volume of EZ-buffer was added, and samples were spun 5min at 500g, resuspended in NSB (1087.5 µl 1XPBS, 5.5µl 2% BSA, 1.5 µl RNase Inhibitor) and filtered 3 times through a 0.22 µm strainer. For scATAC-seq, 100,000 nuclei were resuspended in 50 µl tagmentation mix (10X Genomics)).

scATAC-seq library preparation and sequencing

scATAC-seq targeting 4000 cells per sample was performed using a beta version of Chromium Single Cell ATAC Library and Gel Bead kit (10x Genomics, 1000110) according to the manufacturer's instructions. Libraries were then pooled and loaded on an Illumina NovaSeq sequencer and sequenced to 18,904 median reads per cell for the young dataset and 21,139 median reads per cell for the old dataset. Sequencing data was initially quality controlled and pre-processed using the 10X Genomics CellRanger framework.

31

scATAC-seq analysis of young and old liver tissue

Region accessibility count data were analyzed using the *cisTopic* library *(V. 3.0*[39]. Cells without any accessible regions were removed, leaving 4838 cells from young mice and 3361 cells from old mice. We included 117,290 regions into our analysis that were accessible in at least one cell. The latent Dirichlet allocation model was learned by the *runWarpLDAModels* function for topic numbers ranging from 2 to 15 topics. An appropriate number of topics for our data was selected as the topic number with the highest second derivative of the likelihood function. This was the case for 6 topics, and all downstream analyses use the LDA model learned for 6 topics. Non-linear dimensionality reduction by UMAP was performed for visualization purposes only by applying the built-in *runUmap* function in cisTopic to the topic-distributions of all cells. Topic defining regions were derived via the *getRegionsScores*- and *binarizecisTopics*-function. GO-term and transcription factor motif analysis of the topic defining regions was done using *rGREAT (V.1.22.0)*[76] and *RcisTarget (V.1.10)*[77]. Transcription factor motifs shown in Fig 3F and Fig 6B were downloaded from the *JASPAR* database (http://jaspar.genereg.net).

To check the robustness of the cisTopic results, we performed a complementary analysis of the ame data with *Signac (V.1.0)*[40]. The cell region count matrix was normalized using the term frequency-inverse document frequency (TF-IDF) normalization method from the *Signac* library (*RunTFIDF*). Initial linear dimensionality reduction was performed with singular value decomposition (*RunSVD*). As recoded in the Signac workflow, the first component of the singular value decomposition was excluded from all downstream analyses as it was highly correlated with the sequencing depth. Non-linear dimensionality reduction (UMAP) for Fig. S3A+B was generated via the *RunUMAP* function. The dimensions 2 to 35 were used as input for the algorithm.

Differential accessibility testing

We employed the *FindMarkers* function in the logistic regression framework of[78] to test for regions that were differentially accessible between young and old hepatocytes, respectively, between periportal and pericentral hepatocytes. We considered only regions detected in at

781 least 5% of the cells for testing. P-values were Bonferroni adjusted to account for multiple

782 testing.

Cell type annotation

784 Our celltype annotation is based on the imputed gene activity of known liver cell marker genes

785 from *CellAtlas*[79]. To calculate the imputed gene activities, fragments mapping to gene bodies

786 or promoter regions of genes (Up to 2 kb upstream of a gene) were summed up using the

787 *GeneActivity* function and subsequently normalized via the *NormalizeData* function from

788 Signac. Periportal and pericentral cell populations were annotated based on the gene activity

789 of *Cyp2e1* and *Cyp2f2* genes.

Cell classification via canonical correlation analysis

791 Tabula Muris Senis [9] droplet data were preprocessed as described in the respective section

792 in the manuscript and filtered for cells for male individuals between 3 and 30 months of age.

793 Transfer anchors were determined using the *FindTransferAnchors* function. Cell labels from

794 the tabula Muris droplet dataset were used as provided in the metadata. Cell labels for the

795 scATAC-seq dataset were predicted with the *TransferData* function. For details, see[15].

Construction of Cis-regulatory networks

797 Co-accessibility scores for the interaction network of the *Cidea* locus were predicted with the

798 *Cicero* library[51]. Reduced dimension coordinates of cells were based on the UMAP projection

799 from *cisTopic*. Connections of co-accessible loci were inferred for young and old hepatocytes

800 separately.

801 **Bulk RNA-seq data processing and analysis**

802 The TMS bulk RNA-seq data was analysed as described above by directly using the count

803 matrix provided (https://doi.org/10.6084/m9.figshare.8286230.v1). We only used the data from

804 male mice of the age 3 and 18 months.

805 **scRNA-seq data processing and analysis**

806 *Preliminary processing of TMS data*

807 We downloaded metadata and raw count tables from Tabula Muris Senis consortium for liver

808 FACS and droplets methods. The TMS FACS and droplets data was filtered for genes

33

809   expressed in at least 3 cells, cells containing minimum 250 genes and 2500 counts for droplets

810   while 500 genes and 5000 UMIs for the FACS data. The filtered count matrix was processed

811   using Seurat (4.0.4)[41] with default parameters as per suggested pipeline using

812   'NormalizeData', 'FindVariableFeatures', 'ScaleData', 'RunPCA', 'RunUMAP', 'FindNeighbors'

813   and 'FindClusters' functions. The feature and PCA/UMAP plots generated in this manuscript

814   are through Seurat plotting functions.

815   *Linear model fit of the principal components*

816   We obtained the cell embeddings for each principal component from the processed

817   Seurat objects. The input parameters are principal components, age and animal

818   identity of the cells. The linear model for only hepatocytes was fitted using the 'lm'

819   function in R (4.0.1) as lm(PC_n ~ Age + Mouse.id). The model estimates and

820   predictions were extracted using the R package broom (https://CRAN.R-

821   project.org/package=broom). The model fit with cell types was done in the same

822   manner with "cell type" as an additional factor for cell identity. We tested the increase in

823   noise for significance with 10,000 permutations and compared the actual variance in the old

824   and young cells. This test gave p-values of 0.0002, 0.018 and 0 for the first 3 PCs respectively.

825   *Differential expression and dispersion analysis*

826   The differential analysis was performed using the BASiCS package[56,57]. Posterior

827   estimates were computed using a Markov chain Monte Carlo (MCMC) simulation with 20,000

828   iterations and burn-in period 10000 with a regression model. We used BASiCS to detect

829   differentially expressed and differentially variable genes between old and young hepatocytes.

830   For changes in mean expression between ages, we use the 'BASiCS_TestDE' function with

831   EFDR cutoff 0.1. Only genes with no change in mean expression were considered for

832   interpreting changes in variability. We filtered genes with the detection rate of 0.5 in each

833   age and mean overall expression of 5.

834   Obtained sets of genes from each differentially expressed and variability were further

835   subjected to Gene Ontology Biological Processes enrichment analysis using the 'enrichGO'

34

836   function from clusterProfiler (3.14.3) R package[72]. To remove the redundancy of enriched

837   terms, we used the 'simplify' function from clusterProfiler with the default parameters. The

838   pathway enrichment was performed using the 'enrichPathway' function from the ReactomePA

839   R package (1.36.0)[80].

840

DATA AVAILABILITY

841

842   All sequencing data generated for this study is available at ENA under curation. H3K27ac for

843   young   and   old   mice   was   downloaded   from

844   https://www.ncbi.nlm.nih.gov/bioproject/?term=PRJNA281127[81]. Tabula Muris senis single

845   cell data is available at: https://www.ncbi.nlm.nih.gov/geo/query/acc.cgi?acc=GSE149590[9].

846   Tabula   Muris   senis   bulk   RNA-seq   data   is   available   at:

847   https://www.ncbi.nlm.nih.gov/geo/query/acc.cgi?acc=GSE132040[9].

848

AUTHOR CONTRIBUTIONS

849

855

CONFLICT OF INTEREST

856

857   The authors do not declare any conflict of interest

858

ACKNOWLEDGMENTS

859

873

REFERENCES

875   1.   López-Otín, C., Blasco, M. A., Partridge, L., Serrano, M. & Kroemer, G. The hallmarks

876   of aging. *Cell* **153**, 1194–1217 (2013).

877   2.   Ferrucci, L. & Kuchel, G. A. Heterogeneity of Aging: Individual Risk Factors,

878   Mechanisms, Patient Priorities, and Outcomes. *J. Am. Geriatr. Soc.* **69**, 610–612

879   (2021).

880   3.   Bahar, R. *et al.* Increased cell-to-cell variation in gene expression in ageing mouse

881   heart. *Nature* **441**, 1011–1014 (2006).

882   4.   Somel, M., Khaitovich, P., Bahn, S., Pääbo, S. & Lachmann, M. Gene expression

883   becomes heterogeneous with age. *Curr. Biol.* **16**, R359–R360 (2006).

884   5.   Işıldak, U., Somel, M., Thornton, J. M. & Dönertaş, H. M. Temporal changes in the gene

885   expression heterogeneity during brain development and aging. *Sci. Rep.* **10**, 4080

886   (2020).

887   6.   He, X., Memczak, S., Qu, J., Belmonte, J. C. I. & Liu, G.-H. Single-cell omics in ageing:

888   a young and growing field. *Nat Metab* **2**, 293–302 (2020).

889   7.   Ben-Moshe, S. & Itzkovitz, S. Spatial heterogeneity in the mammalian liver. *Nat. Rev.*

890   *Gastroenterol. Hepatol.* **16**, 395–410 (2019).

891   8.   Jungermann, K. & Kietzmann, T. Zonation of parenchymal and nonparenchymal

892   metabolism in liver. *Annu. Rev. Nutr.* **16**, 179–203 (1996).

893   9.   Schaum, N. *et al.* Ageing hallmarks exhibit organ-specific temporal signatures. *Nature*

894   **583**, 596–602 (2020).

895   10. Petr, M. A. *et al.* A cross-sectional study of functional and metabolic changes during

896   aging through the lifespan in male mice. *Elife* **10**, (2021).

897   11. Chung, K. W. Advances in Understanding of the Role of Lipid Metabolism in Aging.

898   *Cells* **10**, (2021).

899   12. Schleicher, J., Dahmen, U., Guthke, R. & Schuster, S. Zonation of hepatic fat

900   accumulation: insights from mathematical modelling of nutrient gradients and fatty acid

901   uptake. *J. R. Soc. Interface* **14**, (2017).

902   13. Halpern, K. B. *et al.* Single-cell spatial reconstruction reveals global division of labour in

903   the mammalian liver. *Nature* **542**, 352–356 (2017).

904   14. McIntosh, A. L. *et al.* Direct interaction of Plin2 with lipids on the surface of lipid droplets:

905   a live cell FRET analysis. *Am. J. Physiol. Cell Physiol.* **303**, C728-42 (2012).

906   15. Stuart, T. *et al.* Comprehensive Integration of Single-Cell Data. *Cell* **177**, 1888-1902.e21

907   (2019).

908   16. Zhang, M. J., Pisco, A. O., Darmanis, S. & Zou, J. Mouse aging cell atlas analysis

909   reveals global and cell type-specific aging signatures. *Elife* **10**, e62293 (2021).

910   17. Finak, G. *et al.* MAST: a flexible statistical framework for assessing transcriptional

911   changes and characterizing heterogeneity in single-cell RNA sequencing data. *Genome*

912   *Biol.* **16**, 278 (2015).

913   18. Shannon, P. *et al.* Cytoscape: a software environment for integrated models of

914   biomolecular interaction networks. *Genome Res.* **13**, 2498–2504 (2003).

915   19. Bindea, G. *et al.* ClueGO: a Cytoscape plug-in to decipher functionally grouped gene

916   ontology and pathway annotation networks. *Bioinformatics* **25**, 1091–1093 (2009).

917   20. Hunte, C., Palsdottir, H. & Trumpower, B. L. Protonmotive pathways and mechanisms in

918   the cytochrome bc1 complex. *FEBS Lett.* **545**, 39–46 (2003).

919 21. Kadenbach, B. & Hüttemann, M. The subunit composition and function of mammalian

920   cytochrome c oxidase. *Mitochondrion* **24**, 64–76 (2015).

921 22. Chen, J. *et al.* High-resolution 3D imaging uncovers organ-specific vascular control of

922   tissue aging. *Sci Adv* **7**, (2021).

923 23. Janky, R. *et al.* iRegulon: from a gene list to a gene regulatory network using large motif

924   and track collections. *PLoS Comput. Biol.* **10**, e1003731 (2014).

925 24. Pontoglio, M. Hepatocyte nuclear factor 1, a transcription factor at the crossroads of

926   glucose homeostasis. *J. Am. Soc. Nephrol.* **11 Suppl 16**, S140-3 (2000).

927 25. Bonzo, J. A., Ferry, C. H., Matsubara, T., Kim, J.-H. & Gonzalez, F. J. Suppression of

928   hepatocyte proliferation by hepatocyte nuclear factor 4α in adult mice. *J. Biol. Chem.*

929   **287**, 7345–7356 (2012).

930 26. Wangensteen, K. J., Zhang, S., Greenbaum, L. E. & Kaestner, K. H. A genetic screen

931   reveals Foxa3 and TNFR1 as key regulators of liver repopulation. *Genes Dev.* **29**, 904–

932   909 (2015).

933 27. Matsusue, K. *et al.* Hepatic CCAAT/enhancer binding protein alpha mediates induction

934   of lipogenesis and regulation of glucose homeostasis in leptin-deficient mice. *Mol.*

935   *Endocrinol.* **18**, 2751–2764 (2004).

936 28. Veum, V. L. *et al.* The nuclear receptors NUR77, NURR1 and NOR1 in obesity and

937   during fat loss. *Int. J. Obes. (Lond)* **36**, 1195–1202 (2012).

938 29. Lin, W.-J. *et al.* LipidSig: a web-based tool for lipidomic data analysis. *Nucleic Acids*

939   *Res.* **49**, W336–W345 (2021).

940 30. Tan, S. T., Ramesh, T., Toh, X. R. & Nguyen, L. N. Emerging roles of lysophospholipids

941   in health and disease. *Prog. Lipid Res.* **80**, 101068 (2020).

942 31. Breslow, D. K. & Weissman, J. S. Membranes in balance: mechanisms of sphingolipid

943   homeostasis. *Mol. Cell* **40**, 267–279 (2010).

944 32. Gómez-Fernández, J. C. & Corbalán-García, S. Diacylglycerols, multivalent membrane

945   modulators. *Chem. Phys. Lipids* **148**, 1–25 (2007).

946   33. Erion, D. M. & Shulman, G. I. Diacylglycerol-mediated insulin resistance. *Nat. Med.* **16**,

947   400–402 (2010).

948   34. Li, Z. *et al.* Reducing plasma membrane sphingomyelin increases insulin sensitivity.

949   *Mol. Cell. Biol.* **31**, 4205–4218 (2011).

950   35. Paradies, G., Paradies, V., Ruggiero, F. M. & Petrosillo, G. Role of Cardiolipin in

951   Mitochondrial Function and Dynamics in Health and Disease: Molecular and

952   Pharmacological Aspects. *Cells* **8**, (2019).

953   36. Ben-Moshe, S. *et al.* Spatial sorting enables comprehensive characterization of liver

954   zonation. *Nat Metab* **1**, 899–911 (2019).

955   37. Marchetti, P., Fovez, Q., Germain, N., Khamari, R. & Kluza, J. Mitochondrial spare

956   respiratory capacity: Mechanisms, regulation, and significance in non-transformed and

957   cancer cells. *FASEB J.* **34**, 13106–13124 (2020).

958   38. Hill, B. G. *et al.* Integration of cellular bioenergetics with mitochondrial quality control

959   and autophagy. *Biol. Chem.* **393**, 1485–1512 (2012).

960   39. Bravo González-Blas, C. *et al.* cisTopic: cis-regulatory topic modeling on single-cell

961   ATAC-seq data. *Nat. Methods* **16**, 397–400 (2019).

962   40. Stuart, T., Srivastava, A., Lareau, C. & Satija, R. Multimodal single-cell chromatin

963   analysis with Signac. *bioRxiv* 2020.11.09.373613 (2020)

964   doi:10.1101/2020.11.09.373613.

965   41. Hao, Y. *et al.* Integrated analysis of multimodal single-cell data. *Cell* **184**, 3573-

966   3587.e29 (2021).

967   42. Aizarani, N. *et al.* A human liver cell atlas reveals heterogeneity and epithelial

968   progenitors. *Nature* (2019) doi:10.1038/s41586-019-1373-2.

969   43. Sato, S. *et al.* Circadian Reprogramming in the Liver Identifies Metabolic Pathways of

970   Aging. *Cell* **170**, 664-677.e11 (2017).

971   44. Fanti, M., Singh, S., Ledda-Columbano, G. M., Columbano, A. & Monga, S. P. Tri-

972   iodothyronine induces hepatocyte proliferation by protein kinase A-dependent β-catenin

973   activation in rodents. *Hepatology* **59**, 2309–2320 (2014).

974   45. Pouikli, A. *et al.* Chromatin remodeling due to degradation of citrate carrier impairs

975   osteogenesis of aged mesenchymal stem cells. *Nature Aging* vol. 1 810–825 (2021).

976   46. Reynolds, J. C., Bwiza, C. P. & Lee, C. Mitonuclear genomics and aging. *Hum. Genet.*

977   **139**, 381–399 (2020).

978   47. Xu, L., Zhou, L. & Li, P. CIDE proteins and lipid metabolism. *Arterioscler. Thromb. Vasc.*

979   *Biol.* **32**, 1094–1098 (2012).

980   48. Xu, W. *et al.* Differential Roles of Cell Death-inducing DNA Fragmentation Factor-α-like

981   Effector (CIDE) Proteins in Promoting Lipid Droplet Fusion and Growth in

982   Subpopulations of Hepatocytes*♦. *J. Biol. Chem.* **291**, 4282–4293 (2016).

983   49. Barneda, D. *et al.* The brown adipocyte protein CIDEA promotes lipid droplet fusion via

984   a phosphatidic acid-binding amphipathic helix. *Elife* **4**, e07485 (2015).

985   50. Matsusue, K. *et al.* Hepatic steatosis in leptin-deficient mice is promoted by the

986   PPARgamma target gene Fsp27. *Cell Metab.* **7**, 302–311 (2008).

987   51. Pliner, H. A. *et al.* Cicero Predicts cis-Regulatory DNA Interactions from Single-Cell

988   Chromatin Accessibility Data. *Mol. Cell* **71**, 858-871.e8 (2018).

989   52. Muto, Y. *et al.* Single cell transcriptional and chromatin accessibility profiling redefine

990   cellular heterogeneity in the adult human kidney. *Nat. Commun.* **12**, 2190 (2021).

991   53. Dulken, B. W. *et al.* Single-cell analysis reveals T cell infiltration in old neurogenic

992   niches. *Nature* **571**, 205–210 (2019).

993   54. Yi, W., Lu, Y., Zhong, S., Zhang, M. & Sun, L. A single-cell transcriptome atlas of the

994   aging human and macaque retina. *National Science* (2021).

995   55. Martinez-Jimenez, C. P. *et al.* Aging increases cell-to-cell transcriptional variability upon

996   immune stimulation. *Science* **355**, 1433–1436 (2017).

997   56. Vallejos, C. A., Richardson, S. & Marioni, J. C. Beyond comparisons of means:

998   understanding changes in gene expression at the single-cell level. *Genome Biol.* **17**, 70

999   (2016).

1000   57. Eling, N., Richard, A. C., Richardson, S., Marioni, J. C. & Vallejos, C. A. Correcting the

1001   Mean-Variance Dependency for Differential Variability Testing Using Single-Cell RNA

1002   Sequencing Data. *Cell Syst* **7**, 284-294.e12 (2018).

1003   58. Kusumbe, A. P. *et al.* Age-dependent modulation of vascular niches for haematopoietic

1004   stem cells. *Nature* **532**, 380–384 (2016).

1005   59. Wynne, H. A. *et al.* The effect of age upon liver volume and apparent liver blood flow in

1006   healthy man. *Hepatology* **9**, 297–301 (1989).

1007   60. Gong, J. *et al.* Fsp27 promotes lipid droplet growth by lipid exchange and transfer at

1008   lipid droplet contact sites. *J. Cell Biol.* **195**, 953–963 (2011).

1009   61. Zhou, L. *et al.* Cidea promotes hepatic steatosis by sensing dietary fatty acids.

1010   *Hepatology* **56**, 95–107 (2012).

1011   62. Sans, A. *et al.* The Differential Expression of Cide Family Members is Associated with

1012   Nafld Progression from Steatosis to Steatohepatitis. *Sci. Rep.* **9**, 1–12 (2019).

1013   63. Nassir, F., Rector, R. S., Hammoud, G. M. & Ibdah, J. A. Pathogenesis and Prevention

1014   of Hepatic Steatosis. *Gastroenterol. Hepatol.* **11**, 167–175 (2015).

1015   64. Martinez-Pastor, B., Cosentino, C. & Mostoslavsky, R. A tale of metabolites: the cross-

1016   talk between chromatin and energy metabolism. *Cancer Discov.* **3**, 497–501 (2013).

1017   65. Dai, Z., Ramesh, V. & Locasale, J. W. The evolving metabolic landscape of chromatin

1018   biology and epigenetics. *Nat. Rev. Genet.* **21**, 737–753 (2020).

1019   66. Wiese, M. & Bannister, A. J. Two genomes, one cell: Mitochondrial-nuclear coordination

1020   via epigenetic pathways. *Molecular Metabolism* **38**, 100942 (2020).

1021   67. Nikopoulou, C., Parekh, S. & Tessarz, P. Ageing and sources of transcriptional

1022   heterogeneity. *Biol. Chem.* (2019) doi:10.1515/hsz-2018-0449.

1023   68. Lee, B. P. *et al.* Changes in the expression of splicing factor transcripts and variations in

1024   alternative splicing are associated with lifespan in mice and humans. *Aging Cell* **15**,

1025   903–913 (2016).

1026   69. Heintz, C. *et al.* Splicing factor 1 modulates dietary restriction and TORC1 pathway

1027   longevity in C. elegans. *Nature* **541**, 102–106 (2017).

1028   70. Lai, R. W. *et al.* Multi-level remodeling of transcriptional landscapes in aging and

1029   longevity. *BMB Rep.* **52**, 86–108 (2019).

71. Kelmer Sacramento, E. *et al.* Reduced proteasome activity in the aging brain results in ribosome stoichiometry loss and aggregation. *Mol. Syst. Biol.* **16**, e9596 (2020).

72. Yu, G., Wang, L.-G., Han, Y. & He, Q.-Y. clusterProfiler: an R Package for Comparing Biological Themes Among Gene Clusters. *OMICS: A Journal of Integrative Biology* vol. 16 284–287 (2012).

73. Supek, F., Bošnjak, M., Škunca, N. & Šmuc, T. REVIGO summarizes and visualizes long lists of gene ontology terms. *PLoS One* **6**, e21800 (2011).

74. Kolde, R. Pheatmap: pretty heatmaps. *R package version* (2012).

75. Carlson, M., Falcon, S., Pages, H. & Li, N. org. Mm. eg. db: Genome wide annotation for Mouse. (2015).

76. Gu, Z. *rGREAT*. (Bioconductor, 2017). doi:10.18129/B9.BIOC.RGREAT.

77. Aibar, S. *et al.* SCENIC: Single-cell regulatory network inference and clustering. *Nat. Methods* **14**, 1083–1086 (2017).

78. Ntranos, V., Yi, L., Melsted, P. & Pachter, L. A discriminative learning approach to differential expression analysis for single-cell RNA-seq. *Nature Methods* vol. 16 163–166 (2019).

79. Zhang, X. *et al.* CellMarker: A manually curated resource of cell markers in human and mouse. *Nucleic Acids Res.* **47**, D721–D728 (2019).

80. Yu, G. & He, Q.-Y. ReactomePA: an R/Bioconductor package for reactome pathway analysis and visualization. *Mol. Biosyst.* **12**, 477–479 (2016).

81. Benayoun, B. A. *et al.* Remodeling of epigenome and transcriptome landscapes with aging in mice reveals widespread induction of inflammatory responses. *Genome Res.* **29**, 697–709 (2019).
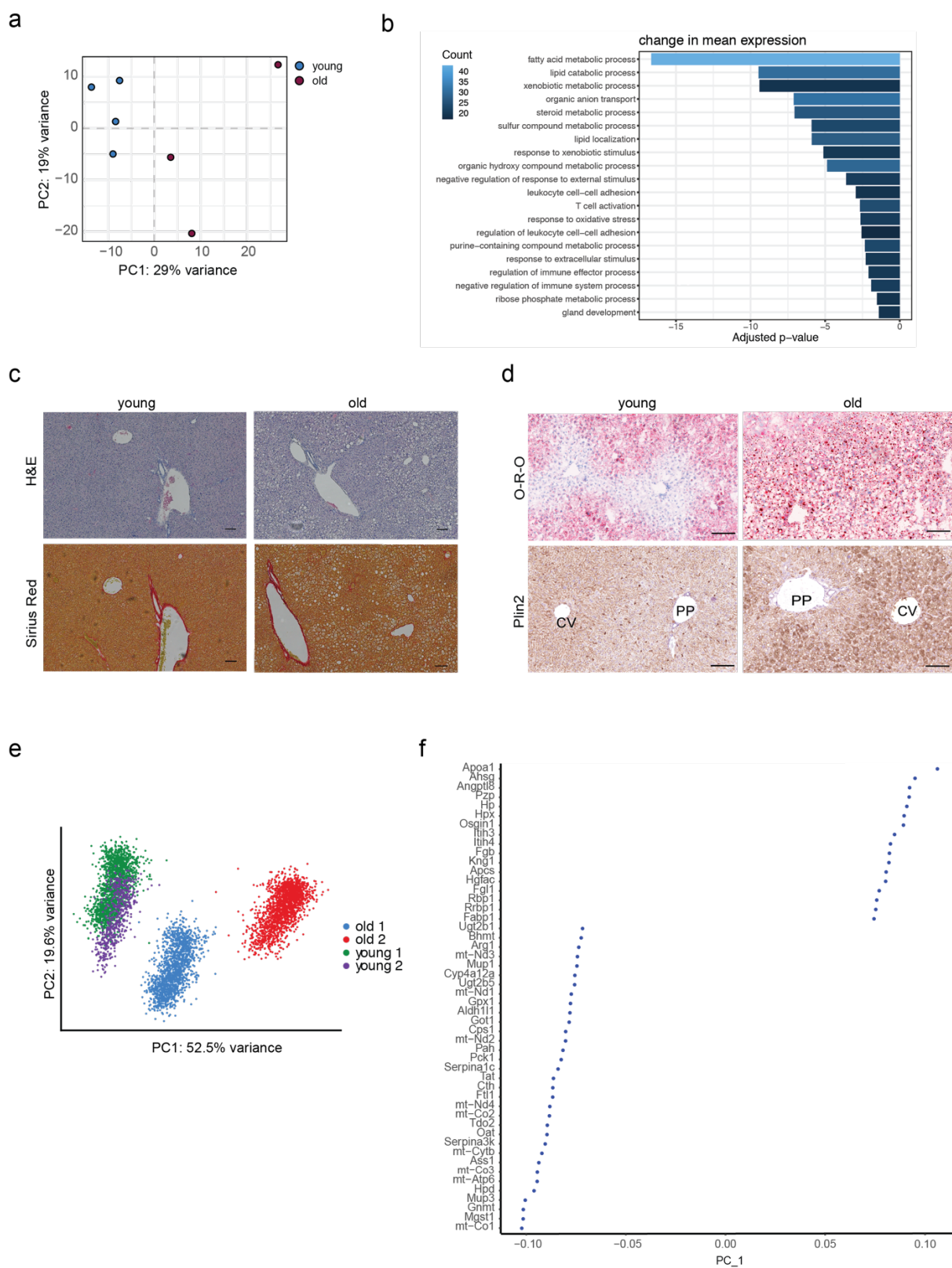
SUPPLEMENTARY FIGURES

Figure S1: a) PCA projection of bulk RNAseq data [9] derived from young and old mouse livers. b) Differentially enriched pathways in the aged liver tissue derived from A (Supplementary Table 1). The

43

1058   colour scale represents the number of genes in each term. c) Representative images from H&E (upper

1059   panel) and Sirius Red (lower panel) stainings on liver sections from a young and an old mouse. Scale

1060   bar=100μm. d) Representative images of PP (periportal) and CV (central vein areas) of Oil-red-O (O-

1061   R-O, upper panel) and Plin2 immunostainings (lower panel) on liver sections from young and old mice.

1062   Scale bar = 100 μm. e) PCA plot of the spatial data after integration of the four datasets using canonical

1063   correlation analysis. Different colours represent the different samples. f) PC plot showing the top 50

1064   genes that separate the ageing groups in Figure S1e.

1065
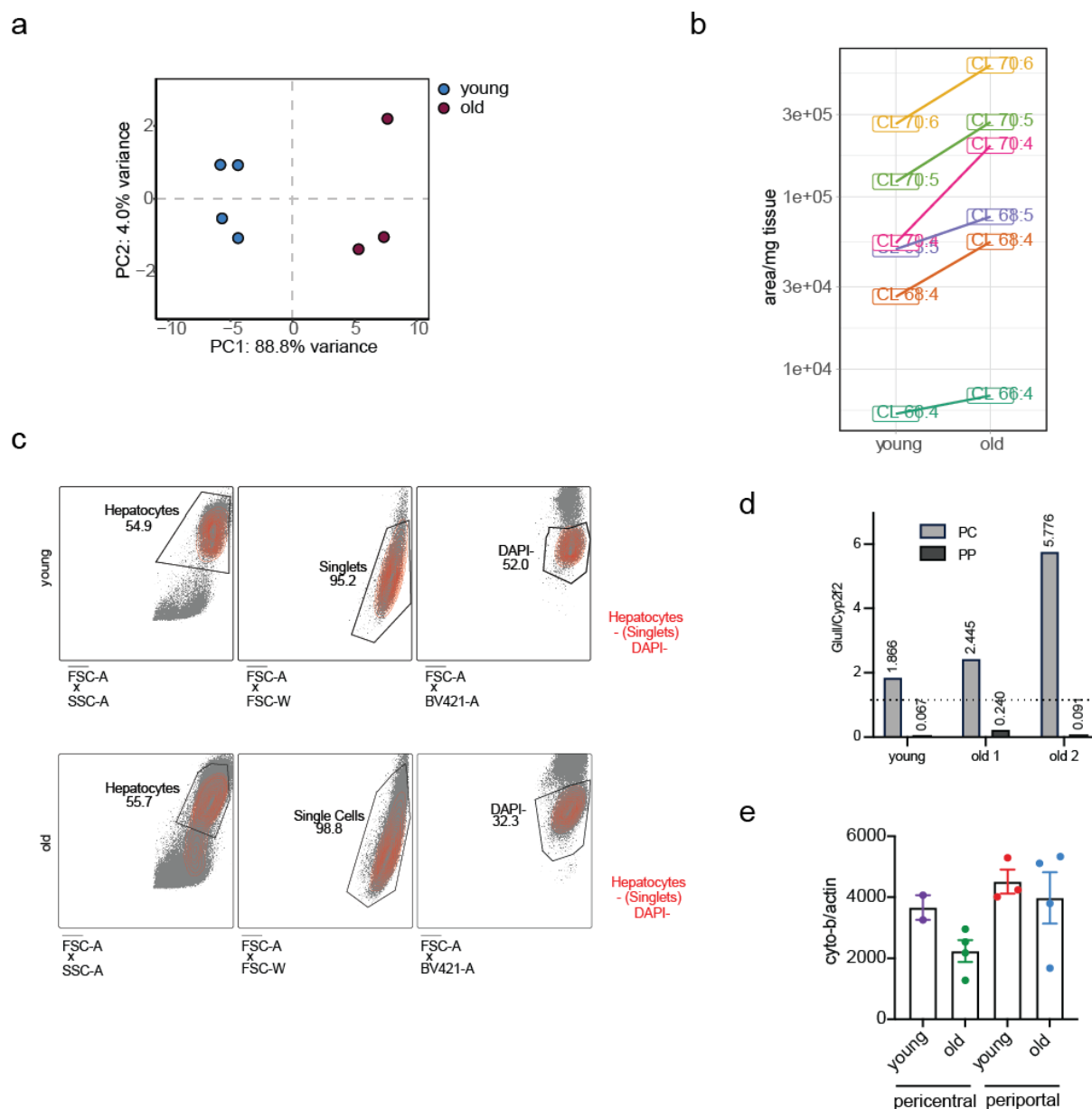
1066

Figure S2: a) PCA of lipidomic data coloured by age. b) Changes of individual cardiolipins between young and old livers. c) Gating strategy for isolation of pericentral and periportal hepatocytes. d) qRT-PCR to validate the enrichment for pericentral and periportal hepatocytes based on expression ratios of Glul and Cyp2f2 levels. Shown are individual replicates for young and old mice (as indicated). e) Mitochondrial content was measured using primers against genomic copies of cyto-b and b-actin. Individual values are given as dots. Error bars represent the SEM.

1073

a

b
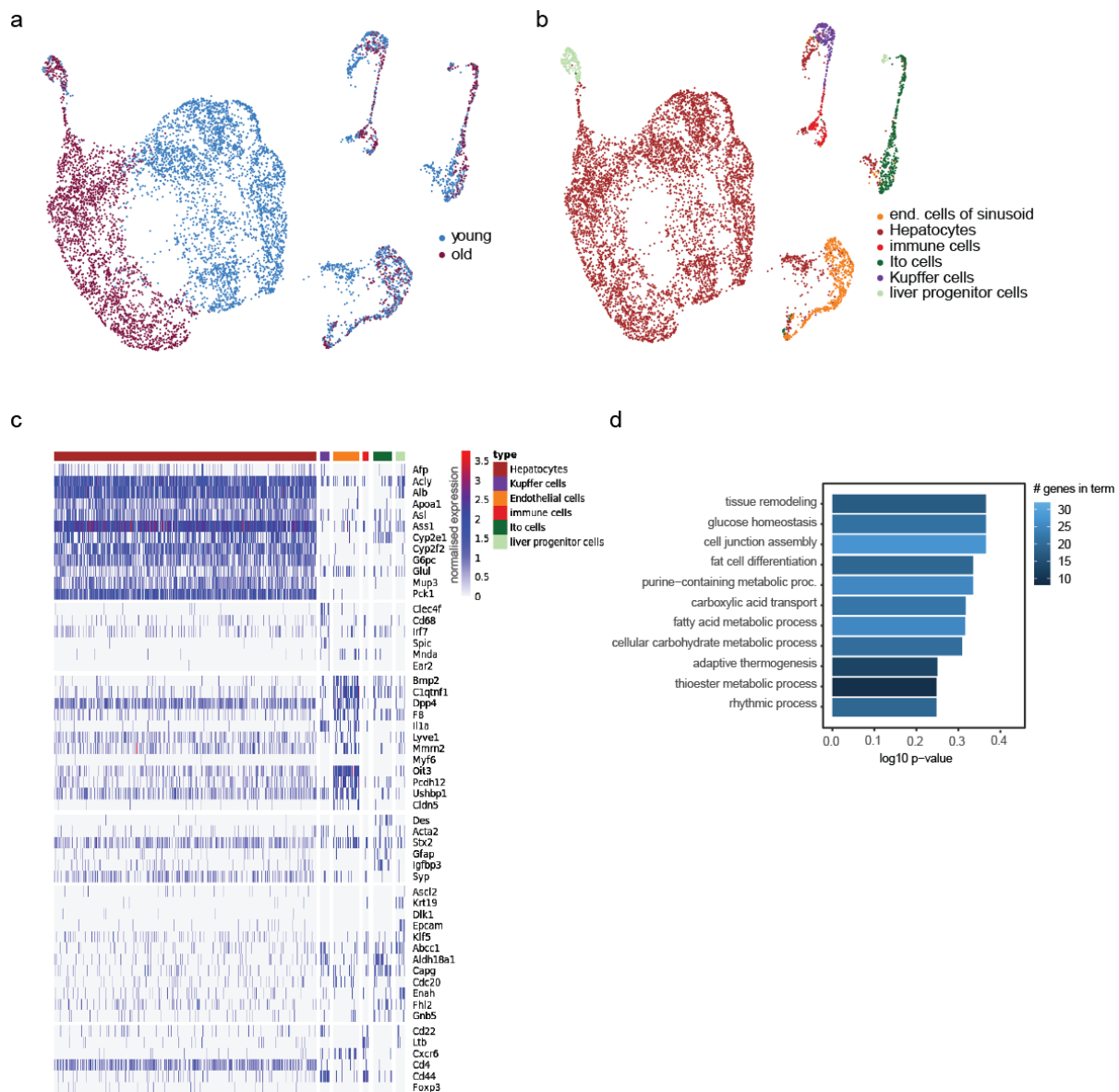
1074

Figure S3: a) UMAP projection of scATAC-seq nuclei from young and old livers. Colour-coded are the different age groups identified using Signac. b) Same as in a). Colour coded are the different cell types, assigned by using marker genes from CellMarker. c) Heatmap showing the accessibility of marker genes in each assigned cell type of the scATAC-seq data. d) GO enrichment for genes found in differentially accessible loci in young vs. old hepatocytes (TSS+/- 3kb).
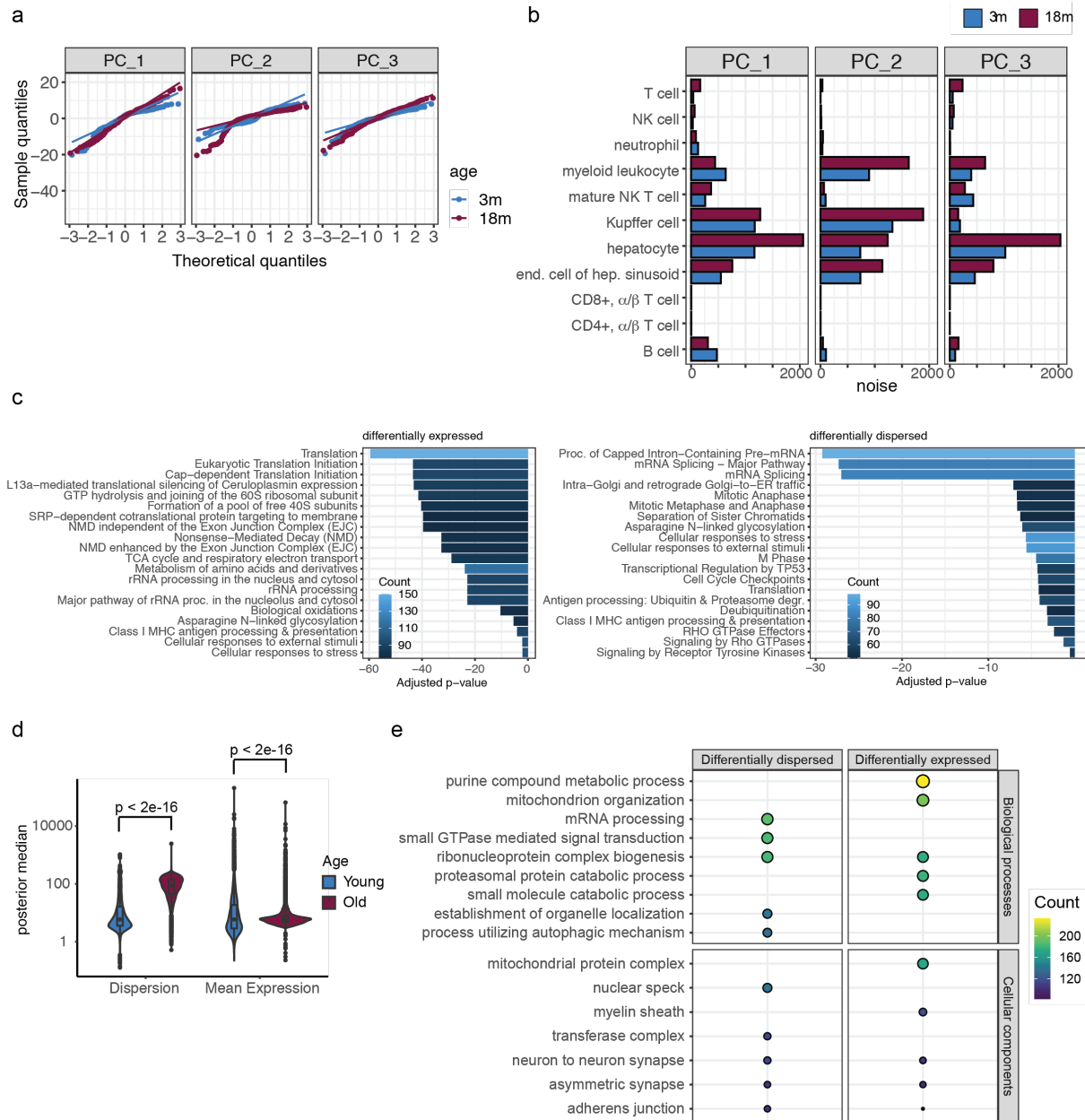
1081
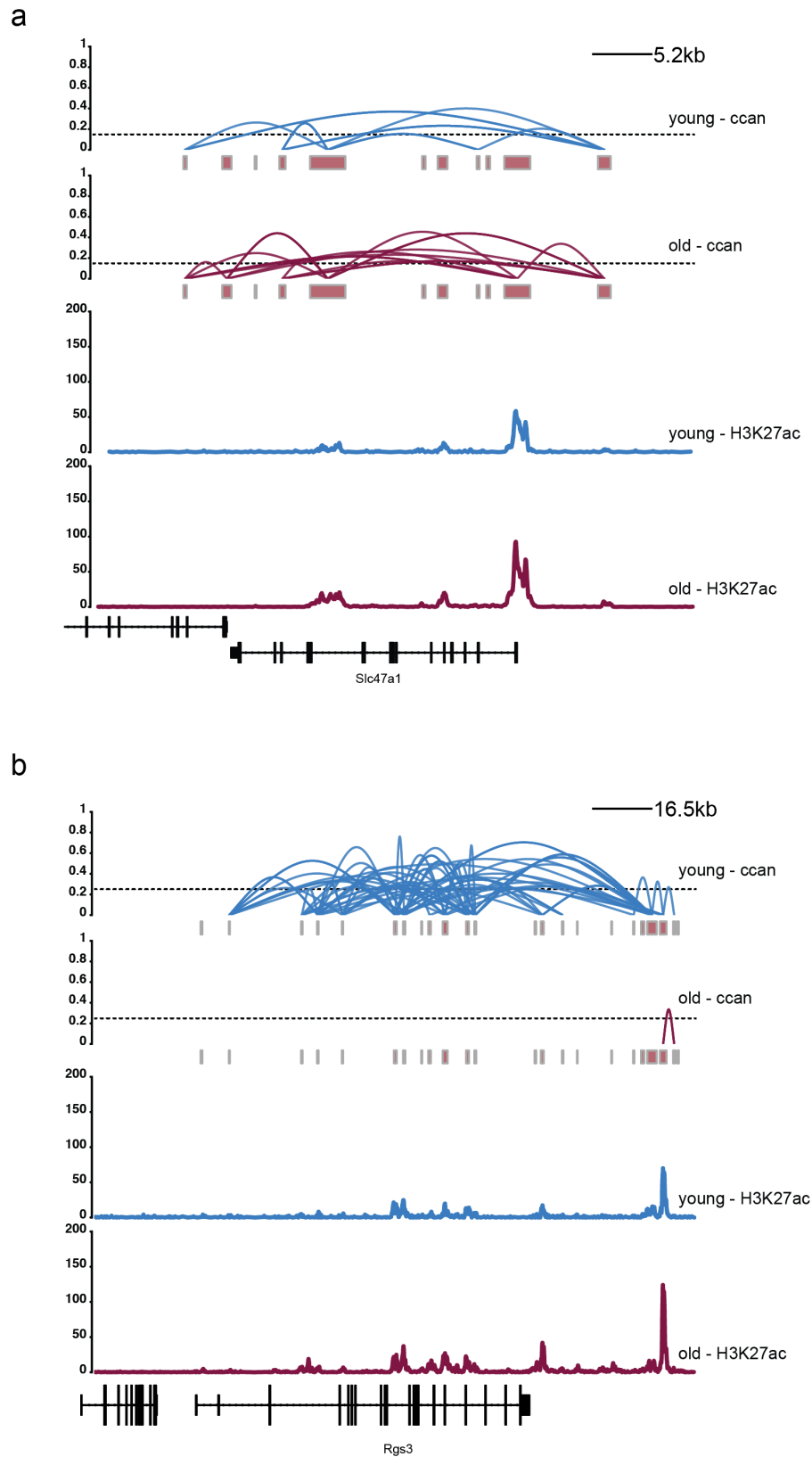
Figure S4: Ccan plots of loci identified to show increased (Slc47a1, a) and decreased (Rgs3, b) co-

accessibility. H3K27ac tracks are shown to indicate potential enhancers.

1084

47

Figure S5: a) QQ-plot of the residuals from a linear model fit for the first 3 PCs with age. b) A barplot of the sum of residual squares (noise) for each linear model fit to the first 5 PCs with age and cell type coloured by age. c) The pathways enrichment for the differentially expressed (left) and differentially over-dispersed (right) genes. d) TMS FACS female data from age 3 and 18 was used to estimate mean expression (mu) and over-dispersion (delta) parameters using a regression model from BASiCS coloured by age. e) Top biological processes (upper panel) and cellular components (lower panel) enriched in the differentially dispersed (left) and differentially expressed (right) genes in the TMS FACS female dataset.
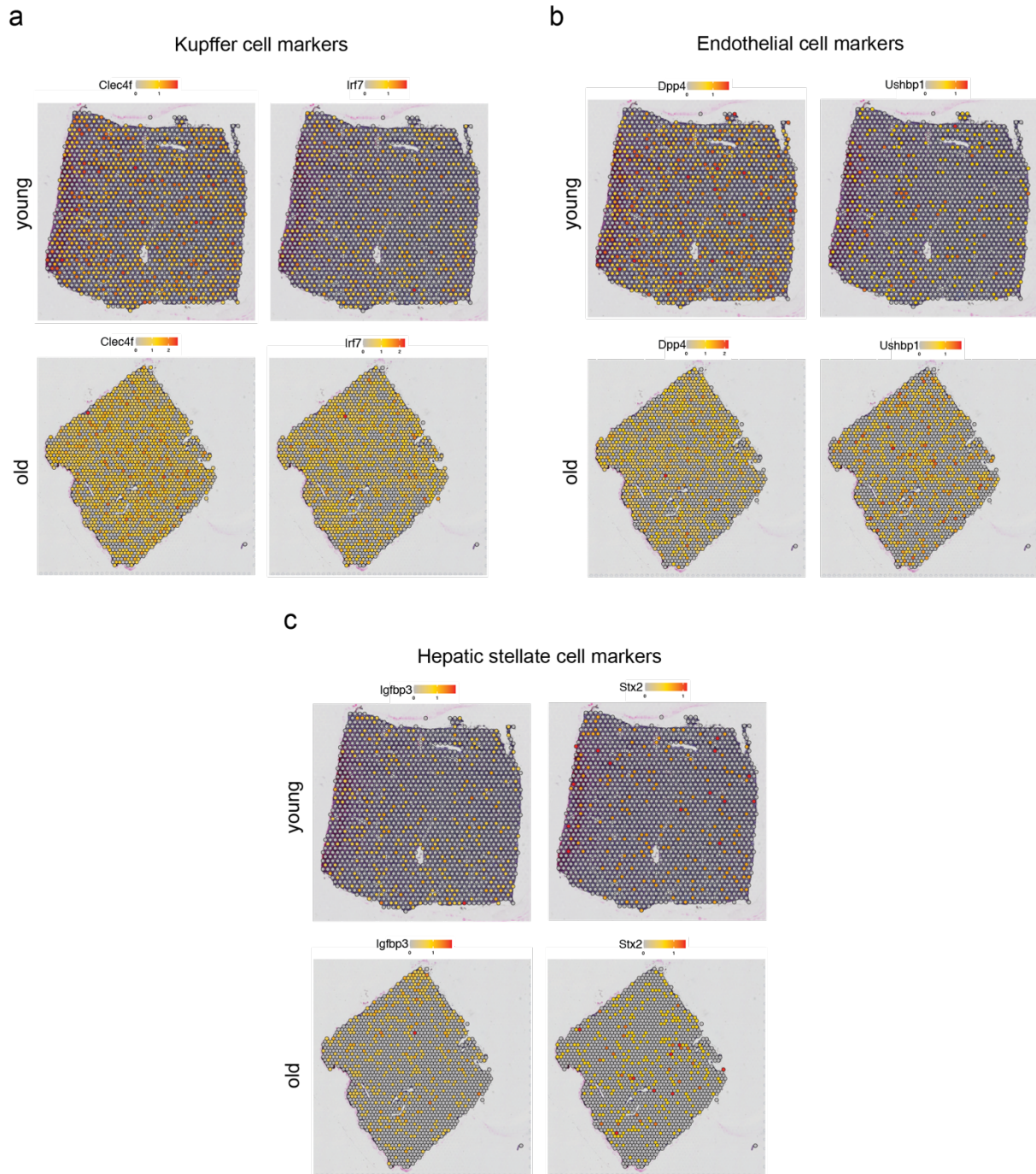
Figure S6: Representative plots showing expression levels of Kupffer cell (a), endothelial cell (b) and hepatic stellate cell (c) markers as indicated in young and old livers as determined by spatial transcriptomics. The colour gradient represents normalised gene expression.